JGR Oceans

RESEARCH ARTICLE
10.1029/2021JC017245

Changing Spatial Patterns of Deep Convection in the Subpolar North Atlantic

Siren Rühs[1,2], Eric C. J. Oliver[1], Arne Biastoch[2,3], Claus W. Böning[2], Michael Dowd[4], Klaus Getzlaff[2], Torge Martin[2], and Paul G. Myers[5]

[1]Department of Oceanography, Dalhousie University, Halifax, Canada, [2]GEOMAR Helmholtz Centre for Ocean Research Kiel, Kiel, Germany, [3]Christian-Albrechts-Universität zu Kiel, Kiel, Germany, [4]Department of Mathematics & Statistics, Dalhousie University, Halifax, Canada, [5]Department of Earth and Atmospheric Sciences, University of Alberta, Edmonton, Canada

Key Points:

- Eddy-rich ocean model simulations (1958–2019) feature large variability of spatial deep convection patterns in subpolar North Atlantic
- In 2015–2018, deep convection showed exceptional large and small relative contributions of eastern and western subpolar gyre, respectively
- Small western contribution is potentially associated with enhanced Greenland melting and recent eastern North Atlantic fresh anomaly

Supporting Information:

Supporting Information may be found in the online version of this article.

Correspondence to:

S. Rühs,
sruehs@geomar.de

Citation:

Rühs, S., Oliver, E. C. J., Biastoch, A., Böning, C. W., Dowd, M., Getzlaff, K., et al. (2021). Changing spatial patterns of deep convection in the subpolar North Atlantic. *Journal of Geophysical Research: Oceans*, *126*, e2021JC017245. https://doi.org/10.1029/2021JC017245

Received 3 FEB 2021
Accepted 2 JUN 2021

Abstract Deep convection and associated deep water formation are key processes for climate variability, since they impact the oceanic uptake of heat and trace gases and alter the structure and strength of the global overturning circulation. For long, deep convection in the subpolar North Atlantic was thought to be confined to the central Labrador Sea in the western subpolar gyre (SPG). However, there is increasing observational evidence that deep convection also has occurred in the eastern SPG south of Cape Farewell and in the Irminger Sea, in particular, in 2015–2018. Here we assess this recent event in the context of the temporal evolution of spatial deep convection patterns in the SPG since the mid-twentieth century, using realistic eddy-rich ocean model simulations. These reveal a large interannual variability with changing contributions of the eastern SPG to the total deep convection volume. Notably, in the late 1980s to early 1990s, the period with highest deep convection intensity in the Labrador Sea related to a persistent positive phase of the North Atlantic Oscillation, the relative contribution of the eastern SPG was small. In contrast, in 2015–2018, deep convection occurred with an unprecedented large relative contribution of the eastern SPG. This is partly linked to a smaller north-westward extent of deep convection in the Labrador Sea compared to previous periods of intensified deep convection, and may be a first fingerprint of freshening trends in the Labrador Sea potentially associated with enhanced Greenland melting and the oceanic advection of the 2012–2016 eastern North Atlantic fresh anomaly.

Plain Language Summary The subpolar North Atlantic is one of the few oceanic regions where deep convection occurs, a process by which surface waters become dense enough to mix downwards. Thereby, heat and carbon dioxide are transported into the deep ocean, helping to slow global warming. For long, deep convection in the subpolar North Atlantic was thought to be confined to the central Labrador Sea. However, recently, deep convection was also observed in the Irminger Sea. In this study, we use ocean model simulations to reconstruct when and where deep convection occurred since the mid-twentieth century. Our simulations show a large variability in strength and spatial patterns of deep convection, with changing relative importance of the Labrador and Irminger Seas. Most notably, in the mid 2010's, deep convection shifted eastwards, so that the relative importance of the Irminger Sea and Labrador Sea were anomalously large and small, respectively. Freshening trends in the Labrador Sea suggest that this shift partially resulted from enhanced melting of Greenland's glaciers and changes in the North Atlantic circulation. Our results stress the need for monitoring and correctly modeling deep convection variability in the Labrador and Irminger Seas to better understand and predict the looming impact of future Greenland melting.

1. Introduction

Oceanic deep convection and the associated deep water formation are key processes for regional to global climate variability, since they largely control the oceans uptake and storage of heat and trace gases such as CO_2 (e.g., Rhein et al., 2017) and alter the structure and strength of the global overturning circulation (Kuhlbrodt & Griesel, 2007; Rhein et al., 2011). Moreover, deep convective mixing enables the transfer of oxygen and organic as well as inorganic matter from the well-ventilated euphotic zone to the deep ocean, and also brings nutrients toward the surface (Severin et al., 2014), thereby largely shaping oceanic ecosystems.

The subpolar North Atlantic constitutes one of the few oceanic regions where deep convection occurs in the open ocean, due to favorable wintertime conditions consisting of a generally weak interior stratification and a cyclonic subpolar gyre (SPG) circulation (associated with doming isopycnals that bring the weakly stratified waters closer to the surface), combined with strong sea-air buoyancy fluxes induced by cold and dry westerly winds (Lab Sea Group, 1998; Marshall & Schott, 1999). The associated convective turbulence allows for regional wintertime mixed layer depths (MLD) deeper than 1000 m, while MLDs in most other oceanic regions are mainly determined by mechanical turbulence driven by wind-stress and on average remain shallower than 150 m (de Boyer Montégut et al, 2004). As a consequence, the subpolar North Atlantic greatly impacts the characteristics of the intermediate and deep waters of the whole Atlantic basin. On the one hand, it enables the local formation of Labrador Sea Water (LSW). On the other hand, it facilitates the transformation of transiting deep waters formed in the Nordic Seas, such as Iceland-Scotland Overflow Water and Denmark Strait Overflow Water through mixing with the overlaying LSW. The resulting water masses, which are eventually exported southward via the Deep Western Boundary Current and interior pathways, are comprehensively referred to as North Atlantic Deep Water (NADW) and form the lower limb of the upper cell of the global overturning circulation in the Atlantic, that is, the Atlantic Meridional Overturning Circulation (AMOC).

In the scientific discussion around ongoing anthropogenic climate change, deep convection in the subpolar North Atlantic has received particular attention for at least two reasons. First, it contributes to the ocean's ability to slow down global warming through the massive uptake and deep storage of excess heat and anthropogenic CO_2 (e.g., Sabine et al., 2004; Terenzi et al., 2007). Second, deep convection in the subpolar North Atlantic is projected to weaken in the course of global warming, for instance, due to increased surface freshwater input as a result of Greenland Ice Sheet melting, which in turn could cause a weakening of the AMOC (e.g., Bakker et al., 2016; Böning et al., 2016).

Longer-term climate trends in deep convection intensity in the subpolar North Atlantic are however superimposed, and hence masked, by interannual-to-decadal variability. The North Atlantic Oscillation (NAO), an index for fluctuations in the strength of the atmospheric pressure gradient between the Azores High and the Icelandic Low (Hurrell & Deser, 2010; Hurrell et al., 2001), is considered the main driver for subpolar deep convection variability on these timescales (Dickson et al., 1996; Lazier, 1980; Ortega et al., 2017). During phases in which the NAO index is positive, westerly winds over the North Atlantic between 40°N and 60°N are particularly strong and lead to more frequent as well as more severe outbreaks of cold and dry air from the North American continent. Subsequently, wintertime heat loss over the SPG is increased, sea surface temperatures are decreased, and the potential for deep convection is enhanced. In addition to this direct NAO response, deep convection variability in the SPG also shows indirect and lagged responses to NAO variability with partially competing effects on upper-ocean buoyancy and water column stability in the subpolar North Atlantic (e.g., Visbeck et al., 2003). These responses involve changes in local and remote sea ice cover (Deser et al., 2000), as well as changes in the strength and size of the SPG, that in turn impact the advection of cold and fresh waters from polar regions versus salty and warm waters from the subtropics (Bersch et al., 2007; Curry & McCartney, 2001; Koul et al., 2020; Lohmann et al., 2009; Sarafanov, 2009). A positive NAO is generally associated with enlarged sea-ice cover in the Labrador Sea, as well as a stronger and eastward extended SPG, that results in a more pronounced doming of isopycnals and the retreat of subtropical waters. The enlarged sea-ice cover in the shelf area locally provides an insulating effect, thereby reducing ocean-to-air heat transfer over the shelf and resulting in even colder air outbreaks over the potential deep convection regions in the interior Labrador Sea and corresponding stronger oceanic heat loss (Schulze et al., 2016). The retreat of subtropical waters enhances the cooling associated with a positive NAO, but also introduces a partially compensating freshening effect in the SPG. This emphasizes an overall dominant role of upper ocean temperature over salinity changes for deep convection variability in the SPG on the associated timescales (Yashayaev & Loder, 2016). Yet, there have been several major surface freshwater disturbances in the SPG, some of which were associated with a temporary shutdown of deep convection (e.g., Gelderloos et al., 2012). These so-called great salinity anomalies (GSAs) were remotely driven by anomalously high sea-ice export from the Arctic via Fram Strait and the East Greenland Current or through Baffin Bay, and occurred in the SPG in the late 1960s to early 1970s, early 1980s, and late 1980s to early 1990s (Belkin, 2004; Belkin et al., 1998; Dickson et al., 1988; Haak et al., 2003). This indicates that deep convection variability in the SPG can be impacted by upper ocean salinity changes not necessarily directly related to NAO variability.

Atmospheric as well as oceanic circulation patterns and hence air-sea buoyancy fluxes as well as heat and freshwater advection can be additionally modulated by other modes of climate variability. For example, the recent (2012–2016) freshening event in the eastern North Atlantic, which has been the largest for the last 120 years (Holliday et al., 2020), is expected to presently arrive in the western North Atlantic with yet unforeseen implications for deep convection.

For a long time, it has been the prevailing view that deep convection in the subpolar North Atlantic predominantly occurs in the western SPG in a relatively confined region in the Labrador Sea, hereafter referred to as the primary deep convection region (Yashayaev, 2007). However, there were early reports (e.g., Nansen, 1912) and a recently increasing number of publications suggesting at least sporadic deep convection also in the eastern SPG south of Cape Farewell and in the Irminger Sea, hereafter referred to as the secondary deep convection regions (Bacon et al., 2003; de Jong et al., 2012, 2018; Falina et al., 2007; Fröb et al., 2016; Kieke & Yashayaev, 2015; Martin & Moore, 2007; Paquin et al., 2016; Pickart, Spall, et al., 2003; Pickart, Straneo, et al., 2003; Pickart et al., 2008; Piron et al., 2016, 2017; Sarafanov, 2009; Sarafanov et al., 2018; Sproson et al., 2008; Våge et al., 2008, 2009; Zunino et al., 2020). In particular, analyses based on Argo data indicate that after a period with mainly low deep convection activity in the 2000s and early 2010s, deep convection resumed in 2015–2018 at the gyre-scale (Piron et al., 2017; Zunino et al., 2020). Some authors suggested that the occurrence of deep convection in the secondary convection regions may be favored by extremely high NAO conditions such as in the early 1990s (Sarafanov, 2009; Sarafanov et al., 2018). Individual deep convection events in the secondary convection regions have been related to local high-frequency wind events (Pickart et al., 2008), for example, Greenland tip-jets (de Jong et al., 2018; Pickart, Spall, et al., 2003; Våge et al., 2008) and reverse tip-jets (Martin & Moore, 2007), cold-air outbreaks from the Labrador coast (Sproson et al., 2008), as well as favorable preconditioning through oceanic advection processes (de Jong et al., 2018; Zunino et al., 2020), some of which may be related to the current state of the NAO (Pickart, Spall, et al., 2003), while others seem to represent independent and/or more local drivers. The exact spatio-temporal patterns of deep convection in the Labrador and Irminger Seas further depend on the activity of mesoscale eddies and filaments that can modify preconditioning as well as restratification processes (e.g., de Jong et al., 2018; Rieck et al., 2019) and may even be impacted by submesoscale processes (Pennelly & Myers, 2020; Tagklis et al., 2020).

In short, a complex interplay of a multitude of factors in the ocean-atmosphere-cryosphere system determine when and where deep convection occurs in the subpolar North Atlantic. Due to its complexity, and despite intense research in the field (Kieke & Yashayaev, 2015), the nature of deep convection variability in the subpolar North Atlantic is still not fully understood and hard to predict (e.g., Våge et al., 2009). In particular, it is not clear how often and to what spatial extent deep convection and associated deep water formation occur outside the primary deep convection region in the central Labrador Sea, that is, in the secondary deep convection regions south of Cape Farewell and in the Irminger Sea. Challenges that need to be overcome are: (i) limited spatio-temporal observational data coverage, which impedes accurate estimates of regional variations in the annual spatial extent and mean depth of deep convection in the different sub-regions, as well as (ii) difficulties in adequately representing deep convection characteristics in ocean model simulations, which requires a high oceanic grid resolution (at least mesoscale eddy resolving) and up-to-date high-resolution atmospheric forcing. Optimally, the latter is capturing both, recent trends in the fresh-water forcing, including increasing runoff and solid discharge from the Greenland Ice Sheet since the mid-1990s (e.g., Bamber et al., 2018), and high-frequency wind events (e.g., Oltmanns et al., 2014).

With this work, we aim at putting the recent observations of gyre-scale intensified convection in 2015–2018 into a broader spatio-temporal context. We assess the temporal evolution of the spatial deep convection pattern in the subpolar North Atlantic since the mid-twentieth century by employing hindcast simulations with the mesoscale eddy-rich ocean/sea-ice model configuration VIKING20X under the established CORE and novel up-to-date JRA55-do atmospheric forcing, and compare our simulation-based results to ARGO observations and previously published literature. Since the process of deep convection itself occurs on very small spatial and temporal scales (e.g., Lab Sea Group, 1998; Marshall & Schott, 1999), it is parametrized in the model and hardly captured by observations. Therefore, we analyze deep convection by its impact on the MLD. A focus is set on the quantification and explanation of changes in the depth and particularly also the spatial extent of deep convection in the Labrador Sea, south of Cape Farewell, and in the Irminger Sea, as

well as the resulting relative contributions to the total annual deep convection volume of the subpolar North Atlantic and associated thermohaline property changes. Our analyses reveal the novelty of the 2015–2018 deep convection pattern and identify first fingerprints of near-surface freshening trends potentially related to the melting of the Greenland ice sheet as well as to the recent eastern North Atlantic fresh anomaly.

The paper is organized as follows: Sections 2.1 and 2.2 describe the employed model simulations and ARGO observations along with the respective MLD diagnostics. Section 2.3 explains the deep convection metrics inferred from the simulated and observed MLDs. Sections 3.1, 3.2 and 3.3 present the simulated variability in MLD and spatial deep convection pattern, the simulated changes in deep convection volume and density, as well as inferred first fingerprints of recent subpolar North Atlantic salinity trends. Sections 4.1, 4.2 and 4.3 discuss the results with respect to an ARGO-based analysis and previously published literature, and reflect on a potential relation to Greenland melting as well as on implications for the larger-scale circulation and climate. Section 5 provides concluding remarks.

2. Material and Methods

2.1. Hindcast Simulations With Eddy-Rich Ocean/Sea-Ice Model Configuration VIKING20X

The VIKING20X model configuration (Biastoch et al., 2021) has been developed at GEOMAR as part of the DRAKKAR initiative (Barnier et al., 2014) and is based on the "Nucleus for European Modeling of the Ocean" version 3.6 (NEMO; Madec & NEMO-team, 2016) with "Océan Parallélisé" as ocean component (OPA; Madec et al., 1998) and "Louvain-la-Neuve Ice Model" version 2 as sea-ice component (LIM2; Fichefet & Maqueda, 1997). It features a tripolar Arakawa C grid (Mesinger & Arakawa, 1976) with a global horizontal resolution of 1/4° that is refined in the Atlantic Ocean between 34°S–70°N to 1/20° via two-way nesting with adaptive grid refinement in Fortran (AGRIF; Debreu et al., 2008). This refinement allows for explicitly resolving mesoscale eddies at subpolar latitudes (Hallberg, 2013). In the vertical the global base and refined nest are composed of 46 z-levels with thickness increasing from 6 m at the surface to maximum 250 m at depth, whereby bottom cells can be partially filled to allow for a more realistic topography (Barnier et al., 2006). VIKING20X is a successor, with updated code and southward extended nest, of the well-established VIKING20 (Behrens, 2013). The eddy-rich resolution of VIKING20 and VIKING20X, hereafter jointly referred to as VIKING20(X), results in a particularly good representation of the North Atlantic circulation patterns, as documented by earlier studies (e.g., Böning et al., 2016; Mertens et al., 2014) and indicated in Figure 1. Moreover, the choice of lateral boundary conditions was identified as a critical aspect for a realistic simulation of eddy kinetic energy (EKE) and deep convection patterns in the Labrador Sea (Rieck et al., 2019). While VIKING20(X) is generally run with a free-slip boundary condition, a no-slip condition is implemented in the West Greenland Current (59–62°N, 43–51°W) to represent the topographic effect on the current necessary to generate Irminger Rings, which travel into the Labrador Sea interior and limit the northward extent of the deep convection area (Figures 1b and S1; also see Marzocchi et al., 2015). Moreover, the nesting approach allows to investigate how regional mesoscale processes alter, or are impacted by, larger scale processes such as the AMOC. Due to these unique features, VIKING20(X) simulations have been employed in a range of studies addressing current issues in physical oceanography, such as the sensitivity of the North Atlantic circulation patterns to increased runoff from Greenland (Böning et al., 2016); the sources and pathways of Denmark Strait Overflow Water (Behrens et al., 2017); the variability of the Deep Western Boundary Current (Fischer et al., 2015; Handmann et al., 2018), North Atlantic Current (Breckenfelder et al., 2017), and North Brazil Current (Rühs et al., 2015); occurrence of benthic storms (Schubert et al., 2018); and the structure and variability of the AMOC (Hirschi et al., 2020).

Past studies with VIKING20(X) mostly relied on hindcast or sensitivity simulations that were forced with the CORE atmospheric data set version 2 (Griffies et al., 2009; Large & Yeager, 2009) available as 6-hourly to monthly fields on a 2° grid for the period 1958–2009, together with climatological monthly varying runoff. However, to be able to address the questions outlined above, an up-to-date and ideally higher resolution forcing that captures recent changes in the runoff is needed. The novel JRA55-do surface data set for driving ocean-sea ice models version 1.4 (Tsujino et al., 2018) based on the Japanese 55-year Reanalysis (Kobayashi et al., 2015) fulfills these criteria. It provides 3-hourly atmospheric forcing data on a 1/2° grid until 2019, together with interannually varying runoff at daily resolution including the effect of accelerated melting of Greenland and Canadian Arctic glaciers as described in Bamber et al. (2018) (note that

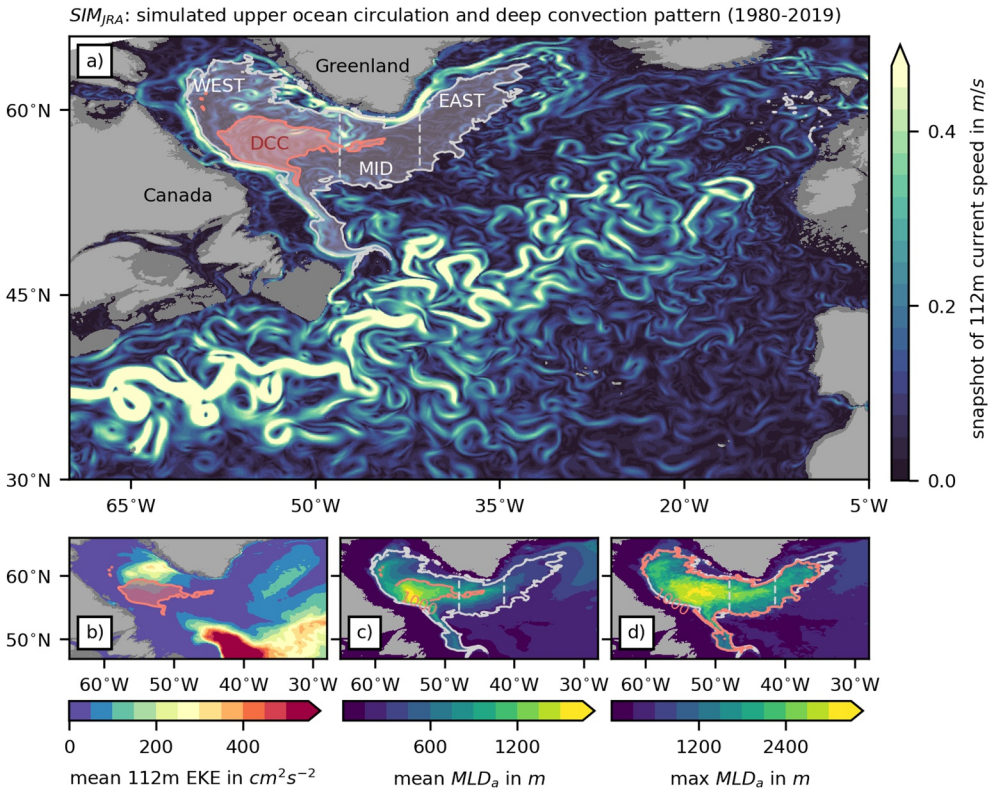

Figure 1. Main features of the North Atlantic circulation and deep convection pattern as simulated with SIM_{JRA} for the period 1980–2019. (a) Snapshot of 5-day mean current speed at 112 m depth (color shading); (b) long-term mean eddy kinetic energy (EKE) at 112 m depth (color shading), calculated based on 5-day mean velocities referenced to the annual mean following Rieck et al. (2015); (c) long-term mean annual maximum mixed layer depth (MLD_a), calculated based on monthly mean MLD, the center of deep convection (DCC) where mean MLD_a exceed z_{crit} = 1000 m is highlighted (light red contour, also added to (a) and (b)); (d) long-term maximum MLD_a, calculated based on monthly mean MLD, the simulation specific potential deep convection region where maximum MLD_a exceed z_{crit} is highlighted (light red contour). In (a), (c) and (d) the light gray contour marks the potential deep convection region determined from SIM_{JRA} and SIM_{CORE} with the three sub-regions in the Labrador Sea (WEST), south of Cape Farewell (MID), and in the Irminger Sea (EAST).

the glacier freshwater flux is only embedded at monthly resolution and solid discharge, that is, calving of icebergs, is converted into liquid runoff). Therefore, in this study, we employ a representative hindcast under CORE forcing ($SIM_{CORE,}$ experiment identifier KKG36013H) together with a complementary short hindcast under JRA55-do forcing (SIM_{JRA}, experiment identifier KKG36107 B). For a 30-year spin-up, the model was initialized with zero velocity fields, temperature and salinity fields from the Polar science center Hydrographic Climatology (PHC, version 2.1; updated from Steele et al., 2001), as well as a representative sea ice field from a previous 1/4° simulation, and then run under CORE forcing for the period 1980–2009. Subsequently, the hindcast SIM_{CORE} was initialized with a snapshot of the oceanic state at the end of the spin-up and run under CORE forcing for the period 1958–2009. Finally, the hindcast SIM_{JRA} was initialized with a snapshot of the simulated oceanic state in SIM_{CORE} at the end of 1979 and run under JRA55-do forcing for the period 1980–2019. Note that for both hindcast simulations the bulk formulae provided by CORE to calculate turbulent air-sea fluxes and a weak sea surface salinity restoring (SSSR) to climatology of 33.33 mm day^{-1} were used. For SIM_{JRA} the SSSR was completely omitted in the coastal zone (80 km) around Greenland to facilitate a potential impact of increased runoff inherent in the novel forcing fields. In the upper ocean, a turbulent kinetic energy (TKE) mixed layer model (Blanke & Delecluse, 1993) was employed, and convection was parameterized by enhanced vertical diffusion (10 m^2 s^{-1}) of tracers and momentum whenever the local Brunt–Väisälä frequency was negative. For a more detailed description and evaluation of the VIKING20X model configuration and the experiments under different atmospheric forcing please refer to Biastoch et al. (2021).

The diagnostics for the MLD that are analyzed in this study are monthly mean values obtained from standard online calculations based on a fixed density threshold method (de Boyer Montégut et al, 2004; Monterey & Levitus, 1997). More specifically, at each model time step and for each grid cell, the MLD was diagnosed as the depth at which the potential density referenced to the surface (σ_0) has changed by 0.01 kg m^{-3} relative to 10 m depth (10 m depth is used as reference to avoid an imprint of diurnal mixed layer changes). Acknowledging that density threshold methods tend to overestimate the MLD (for example due to temperature-salinity compensation which yields a nearly uniform density over a larger depth than temperature and salinity as well as other tracers are actually well mixed), Holte and Talley (2009) introduced a more complex hybrid density algorithm for determining the MLD of ARGO profiles that compares various approaches of MLD estimation and detects the most suitable one. A similar approach has been adopted by Courtois et al. (2017) for ocean models. Here, we deliberately avoid these more complex approaches, since MLD estimates from ARGO observations based on the density algorithm yield qualitatively nearly the same spatio-temporal deep convection variability as estimates based on the density threshold method, aside from an offset in the mean MLD (Figure S2, also see section 2.2 and 2.3).

2.2. ARGO Data

We employ the Argo mixed layer database freely distributed and annually updated at http://mixedlayer.ucsd.edu/ (Holte et al., 2017). This database includes MLD estimates and mixed layer properties (mean density, temperature, and salinity) for more than 2250 000 Argo profiles between 2000 and 2019. MLD estimates were obtained using (i) the Holte and Talley (2009) density algorithm, and (ii) the variable density threshold method introduced by de Boyer Montégut et al. (2004), defining the MLD as the depth at which the density increased by an amount $\Delta\sigma$ that would accompany a temperature drop of 0.2°C referenced to 10 m depth under ambient conditions. This definition translates into a density difference $\Delta\sigma \approx 0.01$ kg m^{-3} for a temperature of 0°C and salinity of 35, and thus, in the region of interest, nicely compares to the fixed density threshold estimate employed in the model simulations (see section 2.1 and 2.3). All main analyses are therefore based on this latter estimate.

2.3. Deep Convection Metrics

The concept of open ocean convection has been thoroughly reviewed in the literature (e.g., Killworth, 1983; Lazier et al., 2001; Marshall & Schott, 1999), but there is no clear definition of the depth level that has to be reached for the classification of *deep* convection. As other authors before us (e.g., Brodeau & Koenigk, 2016; Zunino et al., 2020), we follow the reasoning of Marshall and Schott (1999), who describe deep convection as convection that mixes surface waters deep enough to potentially reset the properties of the abyssal ocean, that is, convection allowing for deep water formation. However, this definition depends on the convection region (and model performance), since different convection regions (and model set-ups) form deep water masses in different depth ranges.

Based on observational data different authors suggested slightly different values for the critical convection depth z_{crit} that needs to be reached in the SPG for the renewal of LSW, ranging between 700 and 1,000 m (see Brodeau & Koenigk, 2016; Piron et al., 2016; Zunino et al., 2020 and references therein). Here we chose $z_{crit} = 1{,}000$ m, accounting for the fact that the employed threshold method used for calculating MLD tends to overestimate real MLDs (based on ARGO data, within the SPG, algorithm-based MLD estimates exceeding 1000 m are on average 315 m deeper than threshold-based estimates for the same profile; also see section 2.1, section 2.2 and Figure S2).

We analyze the simulated interannual deep convection variability based on different spatial aggregates of local annual maximum mixed layer depth (MLD_a). We define the annual deep convection area (DCA_a) as the area spanning all grid points with $MLD_a > z_{crit}$; and the annual deep convection volume (DCV_a) as the corresponding spatial sum of local MLD_a multiplied with the horizontal grid size (similar to, e.g., Tagklis et al., 2020). DCV_a thus represents the mixed layer volume of the annual deep convection region. In addition, we define a potential deep convection region that spans all grid points that experience $MLD_a > z_{crit}$ at least once in at least one simulation (gray contour in Figure 1). This potential deep convection region is further divided into three sub-regions corresponding to the central Labrador Sea (WEST, west of 48°W), the

region south of Cape Farewell (MID, east of 48°W and west of 41.5°W) and the Irminger Sea (EAST, east of 41.5°W), which occasionally show separated deep convection patches in our simulations (Movie S1). The choice of the boundary between the primary and secondary deep convection regions at 48°W is consistent with the choice of Zunino et al. (2020) and further fits to the reported maximum eastern extent of deep convection in the Labrador Sea based on observational data (see. Piron et al. (2017) and references therein); the separation between MID and EAST at 41.5°W is the same as in Piron et al. (2017). Subsequently, moderate and major deep convection periods in the potential deep convection region and sub-regions are inferred via the annual spatial maximum and upper quartile of the spatially varying MLD_a, respectively (similar to the individual profile maximum MLD and spatial aggregate maximum MLD in Yashayaev and Loder (2016, 2017)): years during which at least one grid-point features $MLD_a > z_{crit}$ are considered moderate deep convection years, while years during which more than 25% of the grid points feature $MLD_a > z_{crit}$ are classified as major deep convection years. This analysis was performed for the whole potential deep convection region as well as for all three sub-regions in both model simulations individually, whereby SIM_{JRA} and SIM_{CORE} show a good overall agreement (Figures S4a and S4b). Hence, to simplify comparisons, combined SIM_{JRA} + SIM_{CORE} metrics for periods of major and moderate deep convection periods were established, for which in the overlapping period the criteria must be fulfilled by both simulations (Figure 2e). Note that the timing of the MLD_a shows considerable spatial and temporal variability in the SPG, but nearly all of the grid-points in the potential deep convection region experience their maximum MLD values between January and April (on average 98% and 97% in SIM_{JRA} and SIM_{CORE}, respectively, Figures S3c and S3d) and $MLD_a > z_{crit}$ only occurs between January and April (Figures S3e and S3f). Hence, the derived deep convection metrics can be assigned to a distinct year.

For comparisons with the ARGO data we do not restrict our analysis to annual maximum deep convection depths (which cannot be unambiguously estimated from observations), but include all monthly mean MLDs (MLD_m) > z_{crit}. Also $MLD_m > z_{crit}$ only occurs between January and April and hence allows doing statistics via grouping by distinct years.

Note that in the following, wherever possible, results from SIM_{JRA}/SIM_{CORE} are presented together using this slash notation.

3. Results

3.1. Simulated Variability in Mixed Layer Depth and Spatial Deep Convection Pattern

The simulated long-term (1980–2019/1958-2009) mean MLD_a (Figure 1c for $SIM_{JRA,}$ SIM_{CORE} not shown) features a realistic spatial pattern with a primary center of deep convection (DCC) in the central Labrador Sea, here defined as the region where the long-term mean values exceed z_{crit} = 1000 m. The DCC covers an area of ~166/169 × 10^3 km^2, locally reaches long-term mean depths of up to 1654/1621 m, and—in contrast to most coarser resolution models—is confined in the north through the impact of traveling Irminger Rings resulting in a tongue of elevated EKE also found in observations (Figures 1b and S1, also see Rieck et al., 2019). Similar deep long-term mean MLD_a over a comparable spatial extent cannot be found south of Cape Farewell or in the Irminger Sea. While a long-term mean MLD_a cannot be inferred from observations, a comparison of the simulated (SIM_{JRA}) climatological March MLD for the period 1990–2019 with that inferred from ARGO observations reveals a generally good agreement in the location and spatial extent of the DCCs (red contoured area in Figure S1, the observational DCC extends only slightly less far to the south and slightly farther to the east than the simulated one).

The simulated long-term (1980–2019/1958–2009) maximum MLD_a (Figure 1d for $SIM_{JRA,}$ SIM_{CORE} not shown) reveals, however, that—intermittently—deep convection with depths up to 2800/2876 m and 2133/2674 m also does occur south of Cape Farewell and within the Irminger Sea, respectively. In the Labrador Sea maximum depths up to 3113/3056 m are reached. These values appear larger than the maximum deep convection depths reported from observations (Yashayaev, 2007; Yashayaev & Loder, 2016, 2017). However, it is to note that they represent the single largest values in space and time over the whole simulation, which, even if the model would represent observations perfectly, simply may not be covered by observations. When considering aggregate measures of simulated MLDs, the simulated deep convection depths are quite consistent with observations (see 4.1). Notably—and again in contrast to most coarser resolution

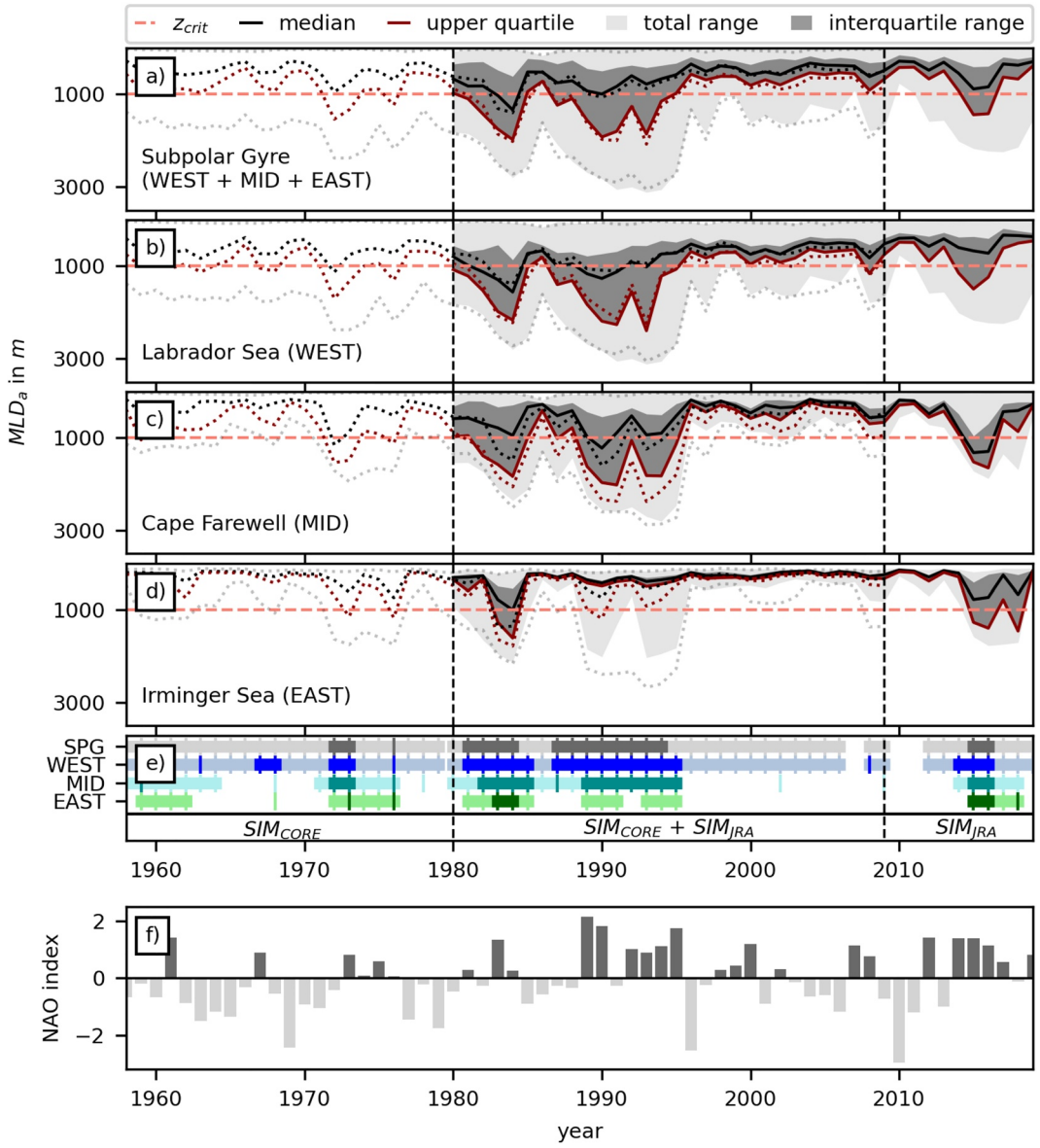

Figure 2. Simulated spatio-temporal variability of annual maximum mixed layer depth (MLD_a). Year-to-year variability of spatial MLD_a aggregates for the potential deep convection region of (a) the whole subpolar gyre, and (b-d) the individual sub-regions WEST, MID, EAST (cf. Figure 1a) as simulated with SIM_{JRA} (solid lines, gray shading) and SIM_{CORE} (dotted lines), the critical depth z_{crit} = 1000 m used to define deep convection is marked by the dashed light red line; (e) overview of defined moderate (light shading, at least one grid point with $MLD_a > z_{crit}$) and major (dark shading, at least 25% of grid-points with $MLD_a > z_{crit}$) deep convection periods, in the overlapping period 1980–2009 the respective criteria must be fulfilled by both simulations; (f) station-based wintertime (DJFM) North Atlantic Oscillation index expressed as anomalies from the 1901–2000 mean, updated version from Jones et al. (1997).

models—simulated deep convection generally does not extend down to the bottom, a layer of lower NADW persists over time (with exceptions for a few grid points at the border of the potential deep convection region that occasionally experience deep convection over the whole water column). The potential deep convection region with long-term maximum $MLD_a > z_{crit}$ spans an area of $932/912 \times 10^3$ km^2 and hence is several times larger than the center of deep convection inferred from long-term mean $MLD_a > z_{crit}$. The pronounced difference between long-term mean and maximum MLD_a in the potential deep convection region reflects the large spatio-temporal variability of the simulated MLD_a.

Before analyzing the details of the spatio-temporal MLD_a and related deep convection variability, we note that the overall characteristics are largely robust between the two hindcast simulations SIM_{CORE} and SIM_{JRA} in their overlapping period between 1980 and 2009 (Figure 2a, Movie S1). Hence, it seems a valid assumption that the combination of both simulations yields an adequate representation of the simulated spatio-temporal MLD_a and inferred deep convection variability between 1958 and 2019. The robustness further indicates that (i) the overall deep convection variability is a forced one with only minor contributions of intrinsic variability, and (ii) the dominant forcing in the overlapping period between 1980 and 2009 is captured by both forcing products. Higher-frequency winds and increasing freshwater input in JRA55-do since the 1990s seem not (yet) to have a significant impact on the overall simulated deep convection variability in the subpolar North Atlantic. The temporal evolution of the MLD_a reveals only minimal deeper MLD_a at the beginning as well as minimal shallower MLD_a at the end of the common period within the Labrador Sea for SIM_{JRA} compared to SIM_{CORE} (Figure 2b). However, SIM_{CORE} has an overall tendency toward slightly deeper MLD_a in the eastern SPG (Figures 2c and 2d). These differences are further discussed in sections 3.2 and 3.3.

The spatio-temporal deep convection variability can be largely described by means of major and moderate deep convection periods (dark and light gray lines in Figure 2e, details for these definitions can be found in section 2.3). We find major periods of deep convection in the early 1970s (only SIM_{CORE}), early 1980s, late 1980s to early 1990s, as well as mid 2010s (only SIM_{JRA}), and moderate deep convection in nearly all of the remaining years—with exception of the years (i) 2007, 2010 and 2011, during which no deep convection with $MLD_a > z_{crit}$ is simulated, and (ii) 1976, which represents an additional individual year with major deep convection. This is largely in line with the results of previous observational-based and modeling studies, even though the spatio-temporal deep convection variability prior to the late 1980s include conflicting reports (for a detailed discussion see section 4.1). It further fits the notion that the overall deep convection variability in the subpolar North Atlantic is linked to the NAO. The wintertime (DJFM) NAO index in its updated version from Jones et al. (1997), expressed as anomalies from the 1901–2000 mean (Figure 2f), shows positive anomalies during all four identified major deep convection periods. However, consistent with the arguments presented by, e.g., Våge et al. (2009) and Courtois et al. (2020), a strong positive NAO anomaly seems neither sufficient nor necessary for the occurrence of individual major deep convection years. On the one hand there exist some years with strong positive NAO anomalies that feature no or only moderate deep convection over a smaller spatial extent (e.g., 1961, 2000, 2007, and 2012). On the other hand, deep convection also occurs during some years with only weekly positive or even negative NAO index (e.g., 1972, 1976, and several years in the early to mid 1980s).

During major deep convection periods, $MLD_a > z_{crit}$ occurs in all three sub-regions, however, at greatly varying spatial pattern and extent (Movie S1). In the Labrador Sea and south of Cape Farewell, $MLD_a > z_{crit}$ is reached for more than 25% of the grid-points in the respective parts of the potential deep convection area during all major deep convection periods (dark blue and dark cyan lines in Figure 2e inferred from Figures 2b and 2c). Notably, and in contrast to the theory proposed by Sarafanov (2009), in the Irminger Sea this threshold was not exceeded in the early 1990s (green lines in Figure 2e inferred from Figure 2d)—the period with the strongest NAO forcing and deepest MLD_a over the SPG as a whole. During the other three major deep convection periods with pronounced Irminger Sea contribution there exist further differences in the spatial deep convection pattern: in the early 1970s and early 1980s deep convection extended farther to the north-west, whereas in the mid 2010s deep convection largely shifted toward the south-east (Movie S1, Figures 3c and 3f). As a result, in the mid 2010s the combined deep convection area of the secondary deep convection regions exceeded that in the Labrador Sea for the first time since 1958 (Figure S5a). In the following period of moderate deep convection, MLD_a decreased faster in the Labrador Sea and south of Cape Farewell than in the Irminger Sea, so that in 2018 deep convection in the Irminger Sea alone surprisingly persisted over a larger area than in the Labrador Sea. During other phases of moderate deep convection, $MLD_a > z_{crit}$ was mainly restricted to the central Labrador Sea and seldomly occurred south of Cape Farewell or within the Irminger Sea, with exceptions around the early 1960s and some years before and after major deep convection periods (Figure 2e).

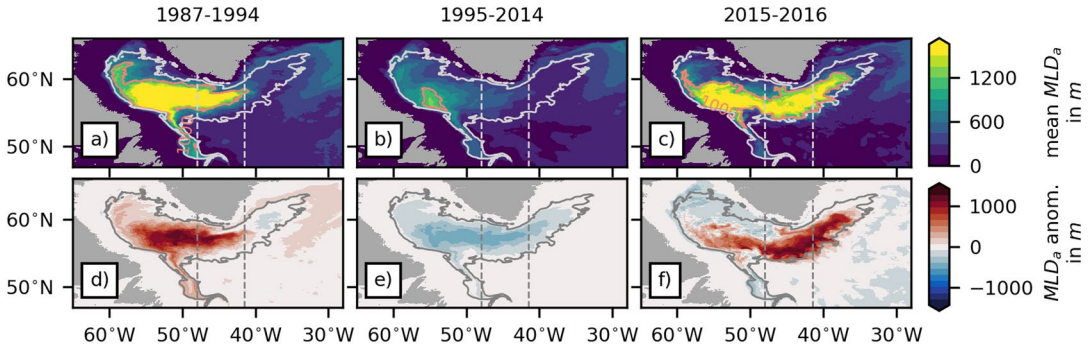

Figure 3. Spatial patterns of mean annual maximum mixed layer depth (MLD_a) (anomalies) during major and moderate deep convection periods since the late 1980s as simulated with SIM_{JRA}. (a–c) Mean MLD_a for major and moderate deep convection periods; (d–f) respective MLD_a anomalies referenced at each location to the long-term (1980–2019) mean MLD_a. Potential (gray contour) and actual (light red contour) deep convection regions are highlighted.

3.2. Simulated Variability in Deep Convection Volume and Density

The simulated eastward shift in the spatial pattern of $MLD_a > z_{crit}$ in the recent major deep convection period compared to previous ones, immediately leads to the question of whether there have been associated changes in the location and density of deep water formation. To gain a first insight into this issue, we analyzed the annual deep convection volume (DCV_a) in the three sub-regions (details for this definition can be found in section 2.3). Assuming that the DCV_a is the maximum volume that could be subducted each year before summer restratification and next winter's deep convection, the maximum annual deep water formation can be estimated by dividing the DCV_a by the number of seconds in a year (i.e., 365*86,400).

The temporal evolution of the absolute DCV_a contributions (Figure 4a) suggest that, occasionally, the DCV_a in the secondary deep convection regions south of Cape Farewell and in the Irminger Sea reaches magnitudes comparable to that of the primary deep convection region in the Labrador Sea during moderate deep convection periods, due to considerable temporary increases in the regional annual deep convection area (Figure S5a). In the Labrador Sea, the DCV_a reaches mean values of $110/135 \times 10^3$ km^3 and $513/470 \times 10^3$ km^3, translating into a maximum annual deep water formation of 3.5/4.3 Sv and 16.3/14.9 Sv, during moderate and major deep convection periods, respectively. Interestingly, the overall maximum DCV_a

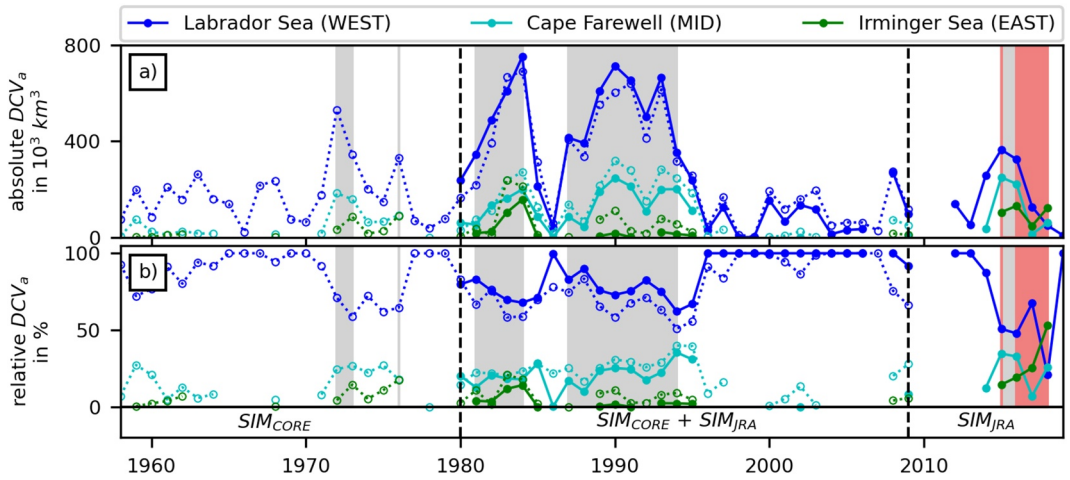

Figure 4. Simulated spatio-temporal variability of deep convection volume. Year-to-year variability of (a) absolute and (b) relative contributions of the three sub-regions WEST, MID, and EAST to the annual deep convection volume (DCV_a) as simulated with SIM_{JRA} (solid lines, filled markers) and SIM_{CORE} (dotted lines, non-filled markers). Gray shading highlights major deep convection periods as defined in Figure 2e and red shading the years 2015–2018 with anomalous large and small relative DCVa contribution of the EAST and WEST deep convection sub-region, respectively.

of 752/691 × 10^3 km^3 (23.8/21.9 Sv), is not reached in the early 1990s, when the spatially averaged deep convection depth is highest (Figure S5b), but in the early 1980s, when the deep convection area is largest. The DCV_a during major deep convection periods in the mid 1970s and mid 2010s are considerably smaller than in the early 1980s and late 1980s to early 1990s, due to shallower depths and smaller spatial extent of deep convection. South of Cape Farewell the DCV_a remains relatively stable around a mean value of 165/188 × 10^3 km^3 (5.2/6.0 Sv) during all major deep convection periods, even though the spatially-averaged deep convection depth shows a large temporal variability comparable in magnitude to that in the Labrador Sea. In the Irminger Sea, the mean DCV_a during major deep convection periods (excluding years without regional deep convection) is only 53/76 × 10^3 km^3 (1.7/2.4 Sv), but in 1983–1984 and 2015–2016 values exceed 100 × 10^3 km^3 (3.2 Sv) due to enlarged spatial extent of deep convection. Most surprisingly, but in line with the MLD_a analysis of section 3.1, the same is true for the year 2018, which features a DCV_a value of 131 × 10^3 km^3 in the Irminger Sea, despite the fact that simulated deep convection intensity over the SPG as a whole only classifies as moderate.

To estimate the potential importance of the individual sub-regions for the overall subpolar deep water formation, we examine the relative DCV_a contributions (Figure 4b). These show a large temporal variability, but feature anomalously large and small contributions of the secondary and primary deep convection regions in 2015–2018, respectively. During major deep convection periods the relative contribution of the Labrador Sea varies from on average 74/65% in the early 1970s and early 1980s, over 77/67% in the late 1980s to early 1990s, to 49% in the mid 2010s. As already indicated by the MLD_a analysis, during most of the moderate deep convection periods, the relative DCV_a contribution of the Labrador Sea is close to 100%—with exceptions for the early 1960s, some years around major deep convection periods, and in 2017–2018. In 2017, for the first time since 1958, the relative DCV_a contribution of the Irminger Sea becomes larger than that of the region south of Cape Farewell, and in 2018 even surpasses that of the Labrador Sea. When comparing the overall temporal evolution of the relative DCV_a contribution of the Labrador Sea with that of the secondary deep convection regions, it becomes apparent that during 2015–2018, in three out of four years, the relative DCV_a contribution of the Labrador Sea falls below 51%, which is unprecedented in SIM_{JRA} and only occurred once before (1994) in SIM_{CORE}. Note that this feature is largely independent of the chosen z_{crit}, as it is already inherent in the temporal evolution of the total mixed volume of the three sub-regions (Figure S6; in all four years the Labrador Sea contribution falls below 58%, which is unprecedented in SIM_{JRA} and only occurred once before in SIM_{CORE}). The anomalous pattern can be related to the evolution of the absolute DCV_a described above: In 2015–2016 the combined absolute DCV_a of the secondary deep convection regions was relatively high, but comparable to that of previous major deep convection periods, while the absolute DCV_a in the Labrador Sea was smaller than during previous major deep convection periods; in 2017 the absolute DCV_a showed a stronger decrease in the Labrador Sea and south of Cape Farewell than in the Irminger Sea; and in 2018 the absolute DCV_a further decreased in the Labrador Sea, while there was a slight recovery in the secondary deep convection regions.

Next to the deep convection volume, the associated densities are of fundamental importance for understanding the potential impacts of deep convection on deep water formation. Our simulations indicate that deep convection in the secondary deep convection regions may enable water mass formation at densities similar to those in the primary deep convection region in the Labrador Sea and hence, as already suggested by various authors before us (e.g., Pickart, Straneo, et al., 2003), potentially contributes to deep water formation.

In the Labrador Sea, the March mixed layer density averaged over the potential deep convection region (Figure 5b) shows largest values in the early 1990s, decreasing values until the early 2010s, and again increasing values until the mid 2010s. The secondary potential deep convection regions experience a similar temporal evolution, though the long-term mean value in the Irminger Sea is much lower than in the Labrador Sea and south of Cape Farewell, since March mixed layer temperatures tend to be higher and salinities tend to be lower during the majority of years (Figures 5d and 5f). March mixed layer densities averaged over the actual deep convection region (Figure 5a) are generally higher than those averaged over the respective potential deep convection region. Moreover, the density difference between the three sub-regions as well as the interannual variability are greatly reduced. This reflects that for deep convection with z_{crit} = 1,000 m to occur, relatively high densities need to be reached. Consequently, during all major deep convection periods,

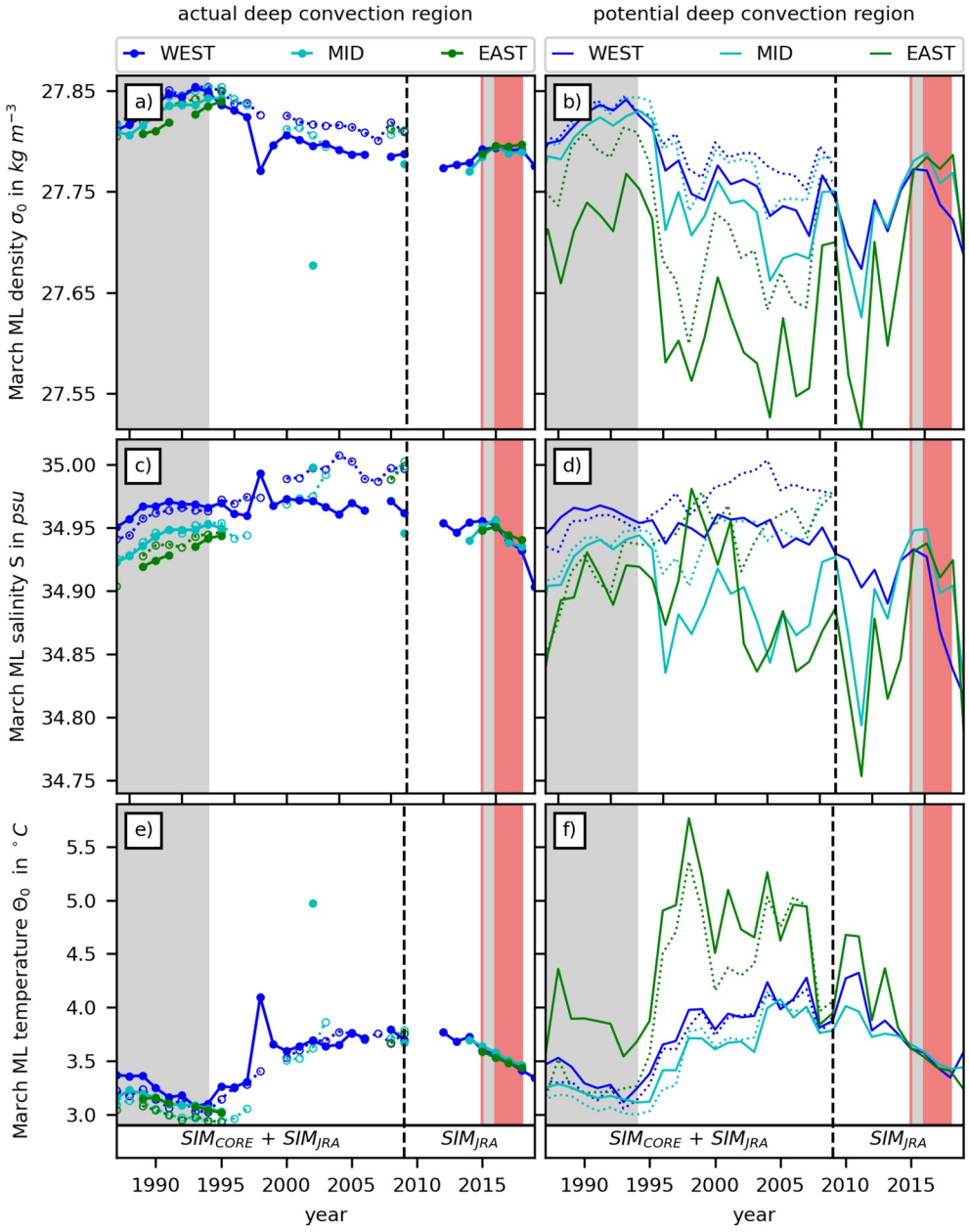

Figure 5. Simulated spatio-temporal variability of March mixed layer (ML) thermohaline properties. Year-to-year variability of volume-weighted spatial average March ML (a–b) potential density anomaly, (c–d) salinity, and (e–f) potential temperature for the actual (lines with markers, left panels) and potential (lines without markers, right panels) deep convection sub-regions as simulated with SIM_{JRA} (solid lines, filled markers) and SIM_{CORE} (dotted lines, non-filled markers). Gray and red background shading as in Figure 4.

deep convection in the primary as well as secondary deep convection regions occurs in the same relative narrow density range. Notably, March mixed layer temperatures averaged over the actual deep convection sub-regions (Figure 5e) feature lower values in the Irminger Sea than in the Labrador Sea (while, as noted above, averaging over the potential deep convection sub-regions yields the opposite). This may be explained by the fact that at lower ambient salinities stronger cooling is needed to reach the required densities and consequently only the coldest profiles make up the actual deep convection region. These analyses highlight that (i) even within our predefined sub-regions thermohaline properties and potential for deep convection greatly varies in space (and time), (ii) newly formed deep water captures the mixed layer properties of win-

ter-time deep convection locations, which are not necessarily representative for a wider sub-region, and, consequently, (iii) the information gained from individual point observations or simple spatial averages alone is limited.

As for the DCV_a, the years 2015–2018 are anomalous with respect to the March mixed layer densities in the three sub-regions. In contrast to previous years, the March mixed layer densities averaged over the potential deep convection region of the Irminger Sea are higher than those of the Labrador Sea. Similarly, in 2016–2018, the March mixed layer densities averaged over the actual deep convection region of the Irminger Sea are higher than those of the Labrador Sea.

Yet, in contrast to the DCV_a and despite the robustness of the general relations and temporal evolution described above, SIM_{JRA} and SIM_{CORE} show non-negligible differences in the spatially averaged March mixed layer densities in their overlapping period after the mid 1980s (during the first years of the common period both simulations match well, which is expected due to the initialization of SIM_{JRA} with SIM_{CORE}). In particular, (i) in the late 1980s to early 1990s densities south of Cape Farewell and especially in the Irminger Sea are lower in SIM_{JRA} than in SIM_{CORE} (densities averaged over the potential deep convection region of the Irminger Sea in SIM_{JRA} do not even reach the maximum in the early 1990s but in the early 1980s); and (ii) after the early 1990s densities in all sub-regions show a stronger decrease in SIM_{JRA} than in SIM_{CORE}. The former seems to be related to regionally and temporarily higher temperatures in SIM_{JRA} compared to SIM_{CORE} and is of minor relevance for this study, whereas the latter appears to be an imprint of different temporal evolutions in the simulated spatially averaged March mixed layer salinity. Specifically, salinities in SIM_{CORE} show positive trends in all sub-regions during the whole simulation period, while salinities in SIM_{JRA} show decreasing trends since the mid 1990s in agreement with a recent observation-based study (Tesdal et al., 2018). These differences can be related to differences in the CORE and JRA55-do forcing data sets and are most likely a result of generally larger freshwater fluxes in JRA55-do compared to CORE, including a more realistic runoff from Greenland (greater magnitude and representation of increase since the mid 1990s, see Figure S9). While the resulting salinity and density changes in SIM_{JRA} seem to have been of minor importance for the overall temporal evolution of MLD_a and DCV_a until the late 2000s, they likely played a role for the development of the anomalous deep convection pattern in 2015–2018 in SIM_{JRA}, as further discussed below.

3.3. Simulated Fingerprints of Recent Subpolar North Atlantic Salinity Trends

A detailed analysis of the simulated March mixed layer salinity and temperature changes averaged over the potential and actual deep convection regions reveals that the recent changes in the spatial deep convection pattern and associated densities are at least partially linked to the simulated regionally differing temporal evolution of upper ocean salinities.

The temporal evolution of March mixed layer salinities averaged over the potential deep convection sub-regions (Figure 5d) shows that the upper Labrador Sea has been freshening between 2000 and 2019 by more than 0.1 psu. This freshening tendency has only been interrupted by a temporary salinity increase in the years 2014–2016 associated with regionally enhanced deep convective mixing. In the Irminger Sea, a similar freshening tendency in the 2000s can be observed, however, superimposed by a larger interannual variability, and further affected by a strong temporary salinity increase between 2011-2016. This salinity increase cannot simply be related to enhanced convective mixing since it sets in before regional MLD_a start to deepen again (see Figure 2d). These regionally different temporal evolutions of March mixed layer salinities contribute to the recently comparatively low and high March mixed layer densities in the Labrador and Irminger Sea, respectively.

March mixed layer salinities averaged over the actual deep convection region (Figure 5c) in the Labrador Sea show a considerably weaker freshening trend than those averaged over the respective potential deep convection sub-region. This may be regarded as a first indication that locations with especially strong freshening did not experience deep convection anymore, which would fit to the above reported smaller regional deep convection area in the mid 2010s compared to the late 1980s to early 1990s.

This hypothesis is further supported by the comparison of the spatial pattern of MLD_a and salinity trends in SIM_{JRA} between 2000 and 2019 (Figures 6a and 6b): MLD_a in the Labrador Sea only deepens in areas where

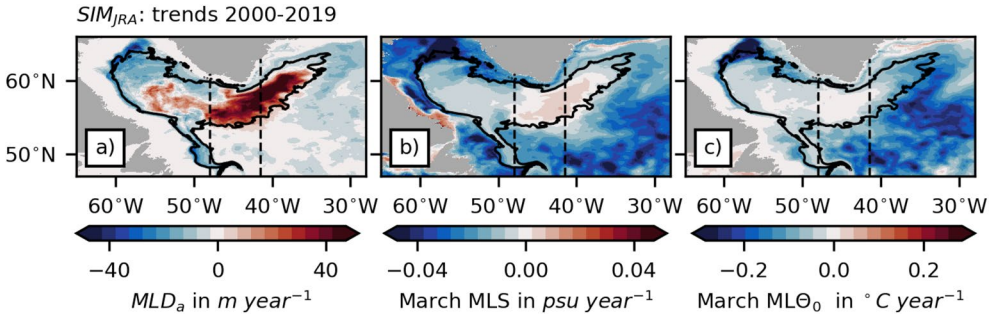

Figure 6. Simulated (SIM_{JRA}) recent linear trends (2000–2019) in (a) annual maximum mixed layer depth (MLD_a), as well as March mixed layer (ML) (b) salinity and (c) potential temperature. The black contour indicates the potential deep convection region.

the freshening is least pronounced. In the Irminger Sea and south of Cape Farewell, where an increase of salinities is observed, MLD_a deepens stronger and over a considerably larger area. In contrast, March mixed layer temperatures (Figure 6c) in the Labrador Sea and south of Cape Farewell reveal deepening MLDa over areas with only weak cooling, and shoaling MLD_a over areas with the strongest cooling. This implies that the spatial pattern in March near-surface temperature trends alone cannot explain the spatial pattern in MLD_a trends, but is at least partially a result of it (a reduction in MLDa implies a smaller volume subject to surface heat loss and hence a stronger temperature drop). Yet, an overall stronger cooling since the 2000s in the Irminger Sea as compared to the Labrador Sea could have contributed to the strong deepening of MLD_a over an anomalously large area in the Irminger Sea.

These analyses indicate that the recent upper ocean freshening trends in the subpolar North Atlantic may have started to impact deep water formation. However, so far, the main impact of these freshening trends seems to be a reduction of the deep convection area in the Labrador Sea and only to a lesser degree a freshening of the locally formed deep waters (with a potential freshening signal getting diluted in areas where deep convective mixing is happening).

4. Discussion

Due to limited spatio-temporal data coverage, the core analyses of this study could not be performed based on observations. Given the still existing large challenges in ocean and climate modeling related to a proper representation of the thermohaline structure and small-scale dynamics in the subpolar North Atlantic, the quantification and attribution of temporal variability in the spatial pattern of deep convection in a state-of-the-art realistic eddy-rich ocean model is certainly valuable on its own. Yet, we argue that the particular value of this study arises from putting recent observational-based findings into a broader spatio-temporal context, thereby revealing the novelty of the 2015–2018 deep convection pattern and linking it to recent upper ocean salinity trends. However, for these findings to be trusted, it is important that the model simulations actually capture the main features of deep convection variability and salinity trends inferred from observations. In addition to the model description and short validation in sections 2.1 and 3.1, we here provide observational evidence for the simulated changes in the deep convection pattern and thermohaline properties in the form of a coherent comparison with ARGO observations and previously published literature. We further critically discuss the potential relation of the simulated changes in the deep convection pattern to the melting of the Greenland ice sheet as well as their implications for the larger-scale ocean circulation and climate, thereby highlighting open questions to be addressed in the future.

4.1. Observational Evidence for Simulated Changes in the Spatial Patterns of Deep Convection and Thermohaline Properties

For a meaningful comparison of the simulated MLD characteristics with those of ARGO data for the period 2000–2019, we analyze the timing, magnitude, spatial extent, and density derived from all simulated monthly mean MLD (MLD_m) > z_{crit} (hence, a certain model grid-point can contribute to the respective

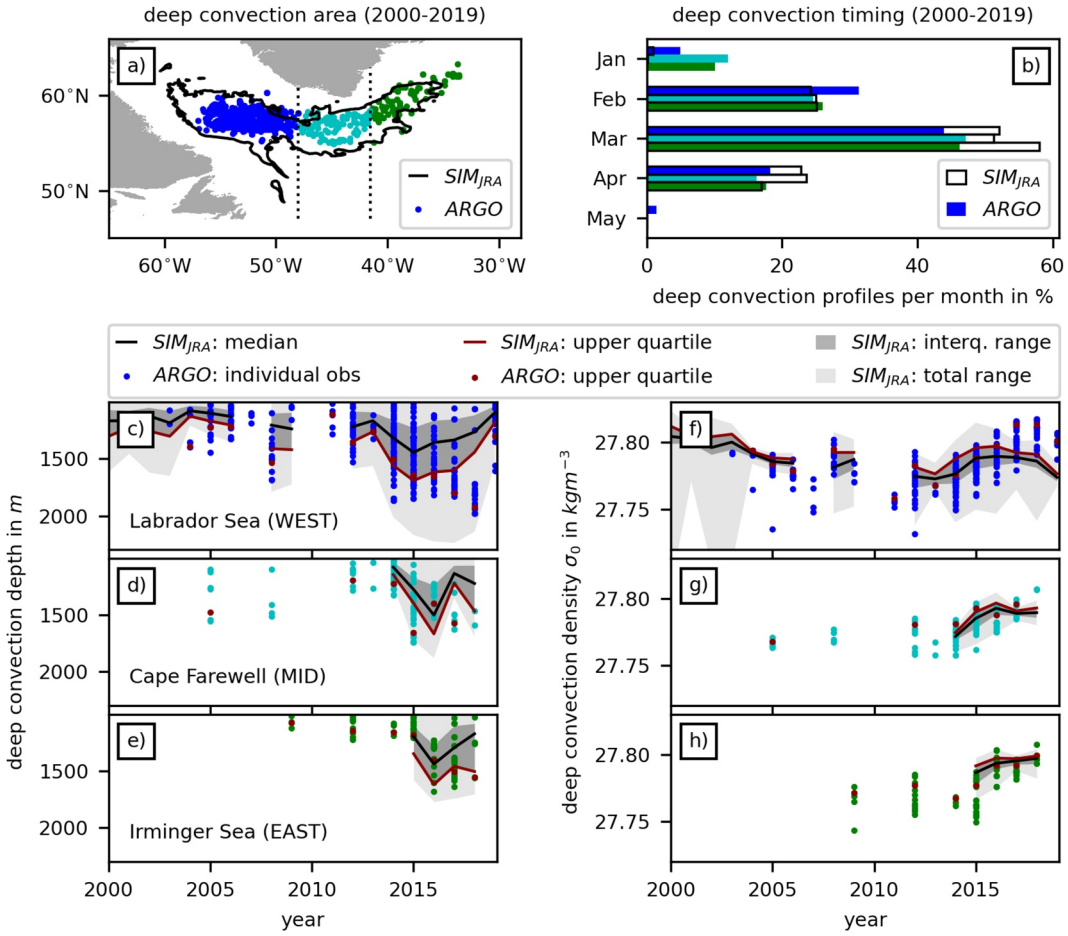

Figure 7. Temporal variability of deep convection characteristics simulated with SIM_{JRA} compared to ARGO observations for the period 2000–2019. (a) Deep convection area, defined in SIM_{JRA} by all grid points that feature monthly mean mixed layer depths (MLD_m) > z_{crit} at least once (black contour), and in ARGO by individual profiles with MLD > z_{crit} (colored dots); (b) deep convection timing visualized by the relative number of deep convection grid points/profiles per month; year-to-year variability of spatial aggregate measures for (c–e) deep convection depths (note: for better comparability with ARGO, all MLD_m > z_{crit} are included instead of only MLD_a > z_{crit}, that is, a certain grid-point can contribute to the statistics more than once per year), and (f–h) associated mixed layer potential density anomaly, whereby a constant offset of 0.05 kg m^{-3} was added to the ARGO observations.

annual statistics more than once per year, in contrast to the main analyses of this study that were based on MLD_a) and from all observational MLD > z_{crit} based on individual ARGO profiles (Figure 7). In ARGO as well as in SIM_{JRA} deep convection with MLD > z_{crit} occurs in all sub-regions from February to April, but most frequently in March (Figure 7b). ARGO observations further report MLD > z_{crit} in January which is not captured in SIM_{JRA} during the period 1980–2009. Yet, when considering the full simulation period, SIM_{JRA} also features deep convection in January and the relative occurrences in March and April are lower, yielding an overall better fit with the ARGO observations (not shown; this indicates a shift in the timing of deep convection in the model simulation). The overall deep convection area in SIM_{JRA}, defined by all grid points that feature simulated MLD_m > z_{crit} at least once during 2000–2019, coincides well with the deep convection area indicated by the spatial distribution of all individual ARGO profiles with MLD > z_{crit} during the same period (Figure 7a). Notably, the deep convection area estimated from ARGO extends slightly farther into the Irminger Sea and slightly less far into the northwestern Labrador Sea. Hence, the relatively large simulated spatial extent of the potential deep convection area in the secondary deep convection regions cannot be discarded as an unrealistic model feature. The simulated deep convection depths also show realistic magnitudes in the primary as well as secondary deep convection regions (Figures 7c–7e). In all three sub-regions the individual ARGO observations mostly fall into the simulated range of deep convection

depths, though in several years during which no deep convection with $MLD_m > z_{crit}$ is simulated, individual ARGO profiles yield MLD > z_{crit} for one or more sub-regions (while there are no years in which the simulation features deep convection without any corresponding evidence from the ARGO observations). This may be regarded as an indication that deep convection depths are generally slightly shallower in SIM_{JRA} than in observations, but also could be the result of the different temporal resolution (simulated monthly means vs. instantaneous profile data) and slight differences in the applied MLD criterion (see sections 2.1 and 2.2). After adding an offset of 0.05 kgm^{-3} to the mixed layer densities inferred from ARGO observations, they, as well, fall into the simulated range, though outliers are more frequent than for deep convection depths (Figures 7f–7h). Here, the different temporal resolution may play an even more important role. The offset in mixed layer densities reflects that simulations with VIKING20(X) generally feature higher than observed salinities in the region of interest, partially compensated by higher than observed temperatures (Handmann et al., 2018)—despite their dynamically good performance. Problems with correctly simulating the salinity in the SPG are well known among ocean models (e.g., Garcia-Quintana et al., 2019; Rattan et al., 2010) and are subject to ongoing model development efforts.

The ARGO data further yields observational evidence for dominant features of the changes in the spatio-temporal deep convection variability inferred from SIM_{JRA}, such as a general increase in deep convection intensity in 2015–2018 compared to the 2000s not only in the Labrador Sea, but also south of Cape Farewell and in the Irminger Sea (Figures 7c–7e, also see Zunino et al. (2020) for a detailed ARGO-based analysis of the processes involved in the 4-year persistence of deep convection in the secondary deep convection regions). Remarkably, not only the range, but also the upper quartile of the simulated and observed deep convection depths shows a relatively good agreement for many years in all three sub-regions (red lines and dots in Figures 7c–7e). This indicates that also the relative frequency of certain deep convection depths within the sub-regions is comparable between simulations and observations. It is notable though that deep convection depths and densities in 2017 and 2018 in the Labrador Sea are slightly deeper and denser in the observations than in the simulations. Yet, we are of the opinion that these differences are not large enough to question our theory of a novel spatial deep convection pattern with increased relative importance of the secondary deep convection regions in 2015–2018, since (i) there are no major differences between observations and simulations in 2015 and 2016, and (ii) while the model simulations may underestimate deep convection depth and/or extent in the Labrador Sea in 2017 and 2018 (the limited spatial distribution of observations does not allow for a conclusive statement in this respect, see Movie S2), deep convection depths and/or extent south of Cape Farewell may likewise be underestimated in 2017, so that the relative contribution of the primary vs. secondary deep convection regions potentially remains unchanged at least in 2017.

The simulated spatio-temporal deep convection variability over the full period of the model hindcasts (1958–2019) can be further compared with the iconic hydrographic timeseries for the central Labrador Sea derived from all available observational data between 1938 and 2016, published and updated by Yashayaev and Loder (2016, 2017). This timeseries shows most intense deep convection periods with strong and deep reaching positive potential density anomalies in the late 1980/early 1990s (1987–1994) and mid 2010s (2014–2016, or 2012–2016 if considering pre-conditioning), which fits nearly perfectly to our definition of the two last regional major deep convection periods (dark blue lines in Figure 2e). In the phase between these two periods, which is characterized by generally lower deep convection intensity, they identify intermittent increases in deep convection intensity in the early 2000s (2000–2003), and in 2008, which are also captured by our simulations (Figure 2b). Despite the general offset between simulated and observed densities, the observed decadal-scale water-column density changes in the order of 0.1 kg m^{-3} between the maximum in the mid 1990s and minimum in the early 2010s and subsequent recovery until 2016 seem to be captured in SIM_{JRA} as indicated in Figure 5a. However, Yashayaev and Loder (2016) do not report increased deep convection intensity in the Labrador Sea during the simulated major deep convection periods in the early 1970s (1972–1973) and early 1980s (1981–1985), but instead in the late 1970s (1977–1978). Interestingly, the two simulated major deep convection periods not captured in the reconstructed observational-based timeseries are associated with positive phases of the NAO and also roughly coincide with the occurrence of two major GSAs in the SPG, while the deep convection period solely identified in the observational-based timeseries is associated with a negative phase of the NAO. In general, this could be interpreted as a tendency of the VIKING20X model configuration toward a too strong and/or direct response of deep convection to changes in the NAO, for example, due to an inadequate representation of the GSAs. However, such an

interpretation would be in strong contrast to the very good agreement of the simulated and observed deep convection variability during the last three decades—including years with high deep convection during negative NAO as well as years with low deep convection during positive NAO. Hence, the disagreements of simulations and observations until the early 1980s may at least partially be a result of limited data availability, evoking, on the one hand, comparatively poor constraints for atmospheric forcing products (in particular with regard to the freshwater components), and, on the other hand, potentially less representative hydrographic observations or reconstructions in the Labrador Sea. For example, in contrast to Yashayaev and Loder (2016) and in better agreement with our and other model simulations (e.g., Böning et al., 2003; Gerdes et al., 2013), Lazier (1980) does report observations of deep convection in the central Labrador Sea with MLD > z_{crit} in 1972–1973.

Not surprisingly, in observations (e.g., Yashayaev and Loder, 2016) as well as in our simulations, temperature variations over the SPG are largely in phase with the regional density variations and mainly correspond to decadal changes in the NAO: After a cooling from 1970s to mid 1990s (not shown), there has been a warming until mid 2010s, followed by another cooling (Figures 5e and 5f). Notably, the recent stronger cooling over the eastern SPG compared to the western SPG (Figures 5f and 6c), which above has been identified as a potential contributor to the anomalous high deep convection intensity in the Irminger Sea, fits to the results of a recent observational-based study by Bryden et al. (2020). Their analyses of EN4 temperature profiles also reveal a stronger cooling in the eastern SPG since 2008, which the authors further link to the reduction of the AMOC and associated heat transport at 26°N. We note that the AMOC at 26°N in our model simulation shows a comparable reduction in AMOC strength over the considered period (Biastoch et al., 2021).

The decadal variability in salinity is less clear. On the one hand, the compilation of hydrographic data for the central Labrador Sea shows that the salinity averaged over the water column between 200 and 2000 m depth also broadly covaries with density and temperature, and—in particular—increased between the mid 1990s until the early 2010s (Yashayaev & Loder, 2017). On the other hand, there is emerging observational evidence for recent upper ocean freshening trends in the subpolar North Atlantic since the early 2000s (Tesdal et al., 2018). The simulated March mixed layer salinity trends in the potential deep convection area in SIM_{JRA} feature a spatial pattern, general timing and magnitude comparable to those upper ocean freshening trends inferred from observation-based products (Tesdal et al., 2018; compare their Figures 9 and 10 with our Figures 5d and 6b). It is important to note though that trends in ocean models should always be interpreted with caution, since ocean models are prone to spurious model drifts—in particular in the subpolar North Atlantic—which may be difficult to distinguish from realistic trends resulting from the forcing. Nevertheless, the good agreement of the simulated changes with recent observational-based estimates is encouraging. Furthermore, as described in section 3.3, the model simulations indicate that the upper ocean freshening trends in the Labrador Sea mainly lead to a reduction of the deep convection area and only to a lesser degree to a freshening of the locally formed deep waters. This may help explain differing views on the temporal evolution of salinity in the Labrador Sea based on surface and hydrographic observations.

4.2. Relation to Melting of the Greenland Ice Sheet

The recent upper ocean freshening trends in the subpolar gyre have been suggested to be at least partially caused by accelerated melting of the Greenland ice sheet (Dukhovskoy et al., 2019; Tesdal et al., 2018; Yang et al., 2016). In agreement with studies exploring the fate of meltwater from Greenland (Böning et al., 2016; Dukhovskoy et al., 2016; Gillard et al., 2016; Luo et al., 2016), the freshening is most pronounced in the boundary current regions and larger in the western SPG than in the eastern SPG.

In section 3.3, we argued that the simulated (SIM_{JRA}) upper ocean freshening trends in the potential deep convection region seem to have contributed to the eastward shift of deep convection in 2015–2018. Hence, given the relatively good agreement between the simulated (SIM_{JRA}) and observed salinity trends (section 4.1), and following the arguments of the above-mentioned previous studies on their relation to Greenland melting, we hypothesize that the anomalous spatial deep convection patterns in 2015–2018 may be partially a result of accelerated Greenland melting.

This hypothesis is supported by the fact that SIM_{CORE}, without interannually varying runoff, does not capture any comparable freshening trend, but instead experiences increasing salinities over the SPG for the

overlapping simulation period until 2009 (dashed lines Figures 5c and 5d). Additionally, and even more importantly, the spatial pattern, timing, and magnitude of the simulated salinity trends in our hindcast experiment SIM_{JRA} are remarkably similar to those trends that can be clearly attributed to Greenland melting derived from the sensitivity experiment presented by Böning et al. (2016) for the period 1990–2019 (compare their Figure 3a and green line in their Figure 3b with our Figure 6 and blue solid line in our Figure 5d). In particular, in the interior Labrador Sea, within both experiments, the salinity remains largely constant until the mid 2000s and then decreases by roughly 0.1 psu until 2019. However, in some regions, the negative salinity trends in the hindcast experiment SIM_{JRA} appear larger than those derived from the sensitivity experiment of Böning et al. (2016); the shelf regions in the northwestern Labrador Sea even showed positive salinity anomalies at the end of the sensitivity experiments, while featuring strong negative trends in the hindcast simulation. This fits to the finding of Dukhovskoy et al. (2019), that freshwater input from Greenland melting alone can not explain the magnitude of the recent observed freshening in the Labrador Sea.

In fact, in SIM_{JRA}, we see first indications that—in addition to Greenland melting—the once-in-a-century freshening of the eastern subpolar North Atlantic in 2012–2016 (Holliday et al., 2020) may have propagated into the western subpolar North Atlantic and subsequently contributed to the pronounced drop in upper ocean salinities in the Labrador Sea in the last years of the simulation (Figure S7): On the one hand, the salinity in the northern Labrador Sea is impacted by variability of the salinity in the East Greenland Current (EGC), in particular its coastal branch (EGCC), which is transferred offshore to the shelf break as its rounds Cape Farewell (Gou et al., 2021) and into the West Greenland Current (WGC), to then be carried by Irminger Rings into the interior (Figures S7b and S8a). The annual mean upper ocean (0–200 m) salinity of the EGC and WGC feature pronounced interannual variability, which mostly originates from the Arctic Ocean (Sutherland et al., 2009), but is increasingly locally influenced by Greenland meltwater. The latter is visible here, for example, by negative peaks in the time series of simulated salinity in 2008–2012 that coincide with largest glacial freshwater input (compare Figure S7b with Figure S9). On the other hand, the salinity in the central to northern Labrador Sea is impacted by signals transmitted through the Irminger Current (IC) passing Cape Farewell (Figure S7c and S8b). The IC features only little variability in the annual mean upper ocean (0–200 m) salinity, except for the last years of the simulation after 2015, when salinity drops to an unprecedented low. We can trace this characteristic drop back upstream the IC and across the Reykjanes Ridge into the eastern North Atlantic at a timescale of a few years. Hence, there has been a two-fold freshening of the north-western Labrador Sea after 2005: A freshening originating from the WGC and EGC with maximum Greenland melting contribution in 2008–2012, combined with a freshening after 2015 related to the arrival of the eastern North Atlantic fresh anomaly. This stabilized the water column and inhibited deep convection in the northern to central Labrador Sea.

A proper quantification of the effect of the recent eastern North Atlantic freshening event and other changes in the freshwater budget versus the effect of Greenland melting on upper ocean salinity trends in the potential deep convection region and the resulting shift in the deep convection pattern is beyond the scope of this study and subject to ongoing analysis.

4.3. Implications for Larger-Scale Ocean Circulation and Climate

To address potential implications of the recent changes in the spatial deep convection pattern for the larger-scale ocean circulation and climate, we analyzed the contributions of the primary and secondary deep convection regions to the total annual deep convection volume in the SPG (section 3.2), which represents an estimate for the upper bound of annual deep water formation via deep convection. We intentionally did not use a more complex definition of deep water formation (e.g., Courtois et al., 2020), since such definitions include other dependencies in addition to deep convection (such as lateral and vertical exchange through the mixed layer base) that need to be disentangled in future studies. We also did not explicitly consider a specific density range for deep water formation. However, the annual total deep convection volume in the SPG populates a relatively confined density range centered around core densities that vary from year to year but are always larger than $\sigma_0 = 27.75$ kg m^{-3}, in the Labrador as well as the Irminger Sea (very similar to the March mixed layer densities averaged over the actual deep convection region shown in Figure 5a). Even when accounting for the above-mentioned offset in the simulated densities compared to the observed ones, the simulated core densities fall well into the observed LSW density range of $\sigma_0 = 27.68$–27.80 kg m^{-3} (e.g.,

Rhein et al., 2002; Rhein et al., 2017). We conclude that in our simulations deep convection in the Labrador Sea as well as the Irminger Sea contribute to LSW formation. Our estimates for the maximum annual LSW formation rates based on the annual deep convection volume can be found at the upper bound of previous estimates for LSW formation based on surface flux timeseries, CFC inventories, hydrographic sections, or output from other numerical model simulations (see for example Garcia-Quintana et al., 2019; Haine et al., 2008, and references therein).

More dedicated studies are required to investigate how much of the deep convection volume is eventually re-entrained into the mixed layer in the following winter and how much actually remains in the deep ocean and finally gets exported to become part of the lower limb of the AMOC, which may be different for the primary and secondary deep convection regions and/or different LSW density classes. This last point is crucial for the understanding of potential larger-scale dynamical impacts of variability in the spatial deep convection pattern. It gains particular relevance in the light of recent publications based on results from the OSNAP program (Lozier et al., 2017) that challenge the classical view of a straight-forward connection between deep convection and associated deep water formation variability in the western subpolar North Atlantic and AMOC strength, and instead point to a much more complex relation largely involving the eastern regions of the subpolar North Atlantic (e.g., Lozier et al., 2019; Menary et al., 2020).

5. Conclusions

In this study we employed hindcast simulations (1958–2019) with a realistic eddy-rich ocean model to assess how often and to what spatial extent deep convection and associated deep water formation in the subpolar North Atlantic occurs outside the primary deep convection region in the central Labrador Sea, that is, in the secondary deep convection regions south of Cape Farewell and in the Irminger Sea. In particular, we put recent observations, indicating that convection intensified over the whole SPG in 2015–2018, into the context of the temporal evolution of the spatial deep convection pattern in the SPG since the mid-twentieth century.

Our study reveals a large temporal variability in the spatial pattern of annual maximum mixed layer depth (MLD_a) and inferred deep convection metrics in the subpolar North Atlantic. In particular, the model simulations feature reoccurred regionally confined deep convection events with $MLD_a > 1000$ m in the secondary deep convection regions. Occasionally, those deep convection events reach a larger spatial extent and potentially allow for deep water formation at a non-negligible rate and in a density range comparable to that of the primary deep convection region, such as in the mid 2010s. Notably, and in contrast to a previous theory, this only happened to a lesser degree (with considerably smaller Irminger Sea contribution) in the late 1980s to early 1990s, the period with highest reported deep convection intensity in the Labrador Sea related to particularly strong NAO forcing. This stresses the point that the intensity of deep convection in the secondary deep convection regions may be partially de-coupled from deep convection intensity in the primary deep convection region and does not follow a simple function of the large-scale atmospheric forcing.

Our study further suggests that the spatial deep convection pattern in 2015–2018 is unprecedented in that the relative contribution of the secondary and primary deep convection regions to the total deep convection volume (DCV_a) in the subpolar North Atlantic has not been as large and small, respectively, since 1958. In the early 1980s deep convection intensity in the Irminger Sea and south of Cape Farewell reached comparable magnitudes, but deep convection intensity in the Labrador Sea was higher, so that the relative DCV_a contribution of the secondary deep convection regions was lower.

Analyses of the temporal evolution of upper ocean salinity in the different sub-regions of the potential deep convection region and the wider North Atantic point at a relationship between the anomalous spatial deep convection pattern in 2015–2018 and near-surface freshening trends in the Labrador Sea since the mid 1990s potentially related to both, enhanced meltwater runoff from Greenland as well as the arrival of the extreme fresh anomaly of the eastern North Atlantic during 2012–2016. Accompanied by a temporary salinity increase between 2011 and 2016 in the potential deep convection region of the eastern SPG and an enhanced cooling in the eastern SPG compared to the western SPG, these salinity changes resulted in a considerably smaller north-westward extent of deep convection in the Labrador Sea and an enlarged deep convection area in the Irminger Sea compared to previous periods of intensified deep convection.

A detailed comparison with ARGO observations for the period 2000–2019 provides confidence that our simulations represent the main characteristics of deep convection in the subpolar North Atlantic in terms of depth, spatial pattern, and timing to a satisfactory degree; and the simulated changes in the upper ocean thermohaline properties are in line with the findings of recent observation-based studies. However, limited data coverage does not allow for any conclusive quantitative analysis of changes in the spatial extent of deep convection and the relative contributions of the individual basins to the total deep convection volume in the subpolar North Atlantic.

Finally, our study motivates the following questions: (1) What is the potential for future occurrences of the 2015–2018 deep convection pattern with increased relative importance of the secondary deep convection regions (in particular considering the suggested stronger effect of continuing Greenland melting on the primary deep convection region)? (2) Are there processes that generally connect or disconnect deep convection intensity in the primary and secondary deep convection regions? (3) What impact do deep convection and associated deep water formation (changes) in the secondary vs. primary deep convection regions have on the AMOC strength (and how do AMOC changes in turn impact the deep convection pattern)? These questions need to be investigated by means of a larger observational data base combining ARGO, moored, and ship-born data, also in form of data assimilation methods; extensive inter-model comparisons at (at least) eddy-rich resolution; as well as dedicated process and sensitivity studies.

Data Availability Statement

For reproducibility of the main results in this study, all (processed) model data and scripts needed for Figures 1–7 are made available using the GEOMAR data management platform under the following publicly available unique identifier: hdl:20.500.12085/adeda524-2145-4daa-9c09-50baf5592e9a. The employed Argo mixed layer database and climatology is freely distributed and annually updated by the University of California San Diego (updated version from Holte et al., 2017, http://mixedlayer.ucsd.edu/, last access: 25 November 2020). The station-based NAO index was re-calculated using sea level pressure data for Gibraltar and Iceland and expressed as anomalies from the 1901–2000 mean, as provided and described by the Climatic Research Unit of the University of East Anglia (updated version from Jones et al. (1997), https://crudata.uea.ac.uk/cru/data/nao/index.htm, last access: 17 December 2020). Global Ocean Gridded sea surface heights and derived variables were made available by E.U. Copernicus Marine Service (CMEMS, product_identifier: SEALEVEL_GLO_PHY_L4_REP_OBSERVATIONS_008_047, https://resources.marine.copernicus.eu/?option=com_csw&product_id=SEALEVEL_GLO_PHY_L4_REP_OBSERVATIONS_008_047&view=details, last access: 15 January 2018).

Acknowledgments
The ocean model simulations and analyses were performed at the High Performance Computing Centers in Berlin/Göttingen (HLRN) and at Kiel University (NESH), Germany. The research was undertaken thanks in part to funding from the Canada First Research Excellence Fund, through the Ocean Frontier Institute, Canada. The study was further supported by the cooperative program "'RACE-Regional Atlantic Circulation and Global Change"' (BMBF Grant 03F0729C). The authors wish to thank the Ocean Dynamics group at GEOMAR and the DRAKKAR consortium for continuous support in setting up and running the model simulations and discussing general model performance issues, Igor Yashayaev and the research group of Paul Myers at the University of Alberta for helpful discussions on the regional oceanography from the observational and modeling point of view, the working groups of Eric Oliver and Michael Dowd at Dalhousie University for critical feedback on analyses and visualization techniques, as well as Willi Rath and Katharina Höflich for technical support. The comments of two anonymous reviewers helped to improve the manuscript.

References

Bacon, S., Gould, W. J., & Jia, Y. (2003). Open-ocean convection in the Irminger Sea. *Geophysical Research Letters*, *30*(5), 1246. https://doi.org/10.1029/2002GL016271

Bakker, P., Schmittner, A., Lenaerts, J. T. M., Abe-Ouchi, A., Bi, D., van den Broeke, M. R., et al. (2016). Fate of the Atlantic Meridional Overturning Circulation: Strong decline under continued warming and Greenland melting. *Geophysical Research Letters*, *43*(23), 12252–12260. https://doi.org/10.1002/2016GL070457

Bamber, J. L., Tedstone, A. J., King, M. D., Howat, I. M., Enderlin, E. M., van den Broeke, M. R., & Noel, B. (2018). Land ice freshwater budget of the Arctic and North Atlantic oceans: 1. Data, methods, and results. *Journal of Geophysical Research: Oceans*, *123*(3), 1827–1837. https://doi.org/10.1002/2017JC013605

Barnier, B., Blaker, A. T., Biastoch, A., Böning, C. W., Coward, A., Deshayes, J., et al. (2014). *DRAKKAR: Developing high resolution ocean components for European Earth system models*. CLIVAR Exchange No 65, *19*(2), 18–21.

Barnier, B., Madec, G., Penduff, T., Molines, J.-M., Treguier, A.-M., Le Sommer, J., et al. (2006). Impact of partial steps and momentum advection schemes in a global ocean circulation model at eddy-permitting resolution. *Ocean Dynamics*, *56*(5-6), 543–567. https://doi.org/10.1007/s10236-006-0082-1

Behrens, E. (2013). *The oceanic response to Greenland melting: The effect of increasing model resolution*. Germany: Christian-Albrechts-Universität zu Kiel.

Behrens, E., Våge, K., Harden, B., Biastoch, A., & Böning, C. W. (2017). Composition and variability of the Denmark Strait Overflow Water in a high-resolution numerical model hindcast simulation. *Journal of Geophysical Research: Oceans*, *122*(4), 2830–2846. https://doi.org/10.1002/2016JC012158

Belkin, I. M. (2004). Propagation of the "Great Salinity Anomaly" of the 1990s around the northern North Atlantic. *Geophysical Research Letters*, *31*(8), 4–7. https://doi.org/10.1029/2003GL019334

Belkin, I. M., Levitus, S., Antonov, J., & Malmberg, S. A. (1998). "Great Salinity Anomalies" in the North Atlantic. *Progress in Oceanography*, *41*(1), 1–68. https://doi.org/10.1016/S0079-6611(98)00015-9

Bersch, M., Yashayaev, I., & Koltermann, K. P. (2007). Recent changes of the thermohaline circulation in the subpolar North Atlantic. *Ocean Dynamics*, *57*(3), 223–235. https://doi.org/10.1007/s10236-007-0104-7

Biastoch, A., Schwarzkopf, F. U., Getzlaff, K., Rühs, S., Martin, T., Scheinert, M., et al. (2021). Regional Imprints of Changes in the Atlantic Meridional Overturning Circulation in the Eddy-rich Ocean Model VIKING20X. *Ocean Science Discussions*. https://doi.org/10.5194/os-2021-37

Blanke, B., & Delecluse, P. (1993). Variability of the tropical Atlantic Ocean simulated by a general circulation model with two different mixed-layer physics. *Journal of Physical Oceanography*, *23*(7), 1363–1388. https://doi.org/10.1175/1520-0485(1993)023<1363:VOTTAO>2.0.CO;2

Böning, C. W., Behrens, E., Biastoch, A., Getzlaff, K., & Bamber, J. L. (2016). Emerging impact of Greenland meltwater on deepwater formation in the North Atlantic Ocean. *Nature Geoscience*, *9*(7), 523–527. https://doi.org/10.1038/ngeo2740

Böning, C. W., Rhein, M., Dengg, J., & Dorow, C. (2003). Modeling CFC inventories and formation rates of Labrador Sea Water. *Geophysical Research Letters*, *30*. https://doi.org/10.1029/2002GL014855

Breckenfelder, T., Rhein, M., Roessler, A., Böning, C. W., Biastoch, A., Behrens, E., & Mertens, C. (2017). Flow paths and variability of the North Atlantic Current: A comparison of observations and a high-resolution model. *Journal of Geophysical Research: Oceans*, *122*(4), 2686–2708. https://doi.org/10.1002/2016JC012444

Brodeau, L., & Koenigk, T. (2016). Extinction of the northern oceanic deep convection in an ensemble of climate model simulations of the 20th and 21st centuries. *Climate Dynamics*, *46*(9–10), 2863–2882. https://doi.org/10.1007/s00382-015-2736-5

Bryden, H. L., Johns, W. E., King, B. A., McCarthy, G., McDonagh, E. L., Moat, B. I., & Smeed, D. A. (2020). Reduction in ocean heat transport at 26°N since 2008 cools the eastern subpolar gyre of the North Atlantic Ocean. *Journal of Climate*, *33*(5), 1677–1689. https://doi.org/10.1175/JCLI-D-19-0323.1

Courtois, P., Garcia-Quintana, Y., Hu, X., & Myers, P. G. (2020). Kinematic subduction rate of Labrador Sea Water from an Eddy-permitting numerical model. *Journal of Geophysical Research: Oceans*, *125*(7), 1–21. https://doi.org/10.1029/2019JC015475

Courtois, P., Hu, X., Pennelly, C., Spence, P., & Myers, P. G. (2017). Mixed layer depth calculation in deep convection regions in ocean numerical models. *Ocean Modelling*, *120*, 60–78. https://doi.org/10.1016/j.ocemod.2017.10.007

Curry, R. G., & McCartney, M. S. (2001). Ocean gyre circulation changes associated with the North Atlantic Oscillation. *Journal of Physical Oceanography*, *31*(12), 3374–3400. https://doi.org/10.1175/1520-0485(2001)031<3374:OGCCAW>2.0.CO;2

de Boyer Montégut, C., Madec, G., Fischer, A. S., Lazar, A., & Iudicone, D. (2004). Mixed layer depth over the global ocean: An examination of profile data and a profile-based climatology. *Journal of Geophysical Research*, *109*(C12), https://doi.org/10.1029/2004jc002378

de Jong, M. F., Oltmanns, M., Karstensen, J., & de Steur, L. (2018). Deep convection in the Irminger Sea observed with a dense mooring array. *Oceanography*, *31*(1), 50–59. https://doi.org/10.5670/oceanog.2018.109

de Jong, M. F., van Aken, H. M., Våge, K., & Pickart, R. S. (2012). Convective mixing in the central Irminger Sea: 2002-2010. *Deep-Sea Research Part I Oceanographic Research Papers*, *63*, 36–51. https://doi.org/10.1016/j.dsr.2012.01.003

Debreu, L., Vouland, C., & Blayo, E. (2008). AGRIF: Adaptive grid refinement in Fortran. *Computers and Geosciences*, *34*, 8–13. https://doi.org/10.1016/j.cageo.2007.01.009

Deser, C., Walsh, J. E., & Timlin, M. S. (2000). Arctic sea ice variability in the context of recent atmospheric circulation trends. *Journal of Climate*, *13*(3), 617–633. https://doi.org/10.1175/1520-0442(2000)013<0617:ASIVIT>2.0.CO;2

Dickson, R., Lazier, J., Meincke, J., Rhines, P., & Swift, J. (1996). Long-term coordinated changes in the convective activity of the North Atlantic. *Progress in Oceanography*, *38*(3), 241–295. https://doi.org/10.1016/S0079-6611(97)00002-5

Dickson, R., Meincke, J., Malmberg, S. A., & Lee, A. J. (1988). The "great salinity anomaly" in the Northern North Atlantic 1968-1982. *Progress in Oceanography*, *20*(2), 103–151. https://doi.org/10.1016/0079-6611(88)90049-3

Dukhovskoy, D. S., Myers, P. G., Platov, G., Timmermans, M. L., Curry, B., Proshutinsky, A., et al. (2016). Greenland freshwater pathways in the sub-Arctic Seas from model experiments with passive tracers. *Journal of Geophysical Research: Oceans*, *121*(1), 877–907. https://doi.org/10.1002/2015JC011290

Dukhovskoy, D. S., Yashayaev, I., Proshutinsky, A., Bamber, J. L., Bashmachnikov, I. L., Chassignet, E. P., et al. (2019). Role of Greenland freshwater anomaly in the recent freshening of the subpolar North Atlantic. *Journal of Geophysical Research: Oceans*, *124*(5), 3333–3360. https://doi.org/10.1029/2018JC014686

Falina, A., Sarafanov, A., & Sokov, A. (2007). Variability and renewal of Labrador Sea Water in the Irminger Basin in 1991–2004. *Journal of Geophysical Research*, *112*, C01006. https://doi.org/10.1029/2005JC003348

Fichefet, T., & Maqueda, M. A. M. (1997). Sensitivity of a global sea ice model to the treatment of ice thermodynamics and dynamics. *Journal of Geophysical Research*, *102*(C6), 12609–12646. https://doi.org/10.1029/97JC00480

Fischer, J., Karstensen, J., Zantopp, R., Visbeck, M., Biastoch, A., Behrens, E., et al. (2015). Intra-seasonal variability of the DWBC in the western subpolar North Atlantic. *Progress in Oceanography*, *132*, 233–249. https://doi.org/10.1016/j.pocean.2014.04.002

Fröb, F., Olsen, A., Våge, K., Moore, G. W. K., Yashayaev, I., Jeansson, E., & Rajasakaren, B. (2016). Irminger Sea deep convection injects oxygen and anthropogenic carbon to the ocean interior. *Nature Communications*, *7*(1), 13244. https://doi.org/10.1038/ncomms13244

Garcia-Quintana, Y., Courtois, P., Hu, X., Pennelly, C., Kieke, D., & Myers, P. G. (2019). Sensitivity of Labrador Sea Water formation to changes in model resolution, atmospheric forcing, and freshwater input. *Journal of Geophysical Research: Oceans*, *124*(3), 2126–2152. https://doi.org/10.1029/2018JC014459

Gelderloos, R., Straneo, F., & Katsman, C. A. (2012). Mechanisms behind the temporary shutdown of deep convection in the Labrador Sea: Lessons from the Great Salinity Anomaly years 1968–71. *Journal of Climate*, *25*(19), 6743–6755. https://doi.org/10.1175/JCLI-D-11-00549.1

Gerdes, R., Hurka, J., Karcher, M., Kauker, F., & Köberle, C. (2013). Simulated history of convection in the Greenland and Labrador Seas, 1948–2001. In H. Drange, T. Dokken, T. Furevik, R. Gerdes, & W. Berger (Eds.), *The Nordic Seas: An Integrated Perspective* (*158*, 221–238). American Geophysical Union. https://doi.org/10.1029/158GM15

Gillard, L. C., Hu, X., Myers, P. G., & Bamber, J. L. (2016). Meltwater pathways from marine terminating glaciers of the Greenland ice sheet. *Geophysical Research Letters*, *43*(20), 10873–10882. https://doi.org/10.1002/2016GL070969

Gou, R., Feucher, C., Pennelly, C., & Myers, P. G. (2021). Seasonal Cycle of the Coastal West Greenland Current System between Cape Farewell and Cape Desolation from a very high-resolution numerical model. *Journal of Geophysical Research: Oceans*, *126*(5), e2020JC017017. https://doi.org/10.1029/2020JC017017

Griffies, S. M., Biastoch, A., Böning, C. W., Bryan, F., Danabasoglu, G., Chassignet, E., et al. (2009). Coordinated Ocean-ice Reference Experiments (COREs). *Ocean Modelling*, *26*, 1–46. https://doi.org/10.1016/j.ocemod.2008.08.007

Haak, H., Jungclaus, J., Mikolajewicz, U., & Latif, M. (2003). Formation and propagation of great salinity anomalies. *Geophysical Research Letters*, *30*(9), 1473. https://doi.org/10.1029/2003GL017065

Haine, T., Böning, C., Brandt, P., Fischer, J., Funk, A., Kieke, D., et al. (2008). North Atlantic deep water formation in the Labrador Sea, recirculation through the subpolar gyre, and discharge to the subtropics. In R. R. Dickson, J. Meincke, & P. Rhines (Eds.), *Arctic-Subarctic Ocean Fluxes* (pp. 653–701). Springer. https://doi.org/10.1007/978-1-4020-6774-7_28

Hallberg, R. (2013). Using a resolution function to regulate parameterizations of oceanic mesoscale eddy effects. *Ocean Modelling*, *72*, 92–103. https://doi.org/10.1016/j.ocemod.2013.08.007

Handmann, P., Fischer, J., Visbeck, M., Karstensen, J., Biastoch, A., Böning, C., & Patara, L. (2018). The deep western boundary current in the Labrador Sea from observations and a high-resolution model. *Journal of Geophysical Research: Oceans*, *123*(4), 2829–2850. https://doi.org/10.1002/2017JC013702

Hirschi, J. J. M., Barnier, B., Böning, C., Biastoch, A., Blaker, A. T., Coward, A., et al. (2020). The Atlantic meridional overturning circulation in high-resolution models. *Journal of Geophysical Research: Oceans*, *125*(4). https://doi.org/10.1029/2019JC015522

Holliday, N. P., Bersch, M., Berx, B., Chafik, L., Cunningham, S., Florindo-López, C., et al. (2020). Ocean circulation causes the largest freshening event for 120 years in eastern subpolar North Atlantic. *Nature Communications*, *11*(1). https://doi.org/10.1038/s41467-020-14474-y

Holte, J., & Talley, L. (2009). A new algorithm for finding mixed layer depths with applications to argo data and subantarctic mode water formation. *Journal of Atmospheric and Oceanic Technology*, *26*(9), 1920–1939. https://doi.org/10.1175/2009JTECHO543.1

Holte, J., Talley, L. D., Gilson, J., & Roemmich, D. (2017). An Argo mixed layer climatology and database. *Geophysical Research Letters*, *44*(11), 5618–5626. https://doi.org/10.1002/2017GL073426

Hurrell, J. W., & Deser, C. (2010). North Atlantic climate variability: The role of the North Atlantic Oscillation. *Journal of Marine Systems*, *79*(3–4), 231–244. https://doi.org/10.1016/j.jmarsys.2009.11.002

Hurrell, J. W., Kushnir, Y., & Visbeck, M. (2001). The north Atlantic oscillation. *Science*, *291*(5504), 603–605. https://doi.org/10.1126/science.1058761

Jones, P. D., Jonsson, T., & Wheeler, D. (1997). Extension to the North Atlantic oscillation using early instrumental pressure observations from Gibraltar and south-west Iceland. *International Journal of Climatology*, *17*(13), 1433–1450. https://doi.org/10.1002/(SICI)1097-0088(19971115)17:13<1433::AID-JOC203>3.0.CO;2-P

Kieke, D., & Yashayaev, I. (2015). Studies of Labrador Sea Water formation and variability in the subpolar North Atlantic in the light of international partnership and collaboration. *Progress in Oceanography*, *132*, 220–232. https://doi.org/10.1016/j.pocean.2014.12.010

Killworth, P. D. (1983). Deep convection in the World Ocean. *Reviews of Geophysics*, *21*(1), 1–26. https://doi.org/10.1029/RG021i001p00001

Kobayashi, S., Ota, Y., Harada, Y., Ebita, A., Moriya, M., Onoda, H., et al. (2015). The JRA-55 reanalysis: General specifications and basic characteristics. *Journal of the Meteorological Society of Japan*, *93*(1), 5–48. https://doi.org/10.2151/jmsj.2015-001

Koul, V., Tesdal, J. E., Bersch, M., Hátún, H., Brune, S., Borchert, L., et al. (2020). Unraveling the choice of the north Atlantic subpolar gyre index. *Scientific Reports*, *10*(1), 1–12. https://doi.org/10.1038/s41598-020-57790-5

Kuhlbrodt, T., Griesel, A., Montoya, M., Levermann, A., Hofmann, M., & Rahmstorf, S. (2007). On the driving processes of the Atlantic meridional overturning circulation. *Reviews of Geophysics*, *45*(2), RG2001. https://doi.org/10.1029/2004RG000166

Lab Sea Group. (1998). The Labrador Sea deep convection experiment. *Bulletin of the American Meteorological Society*, *79*(10), 2033–2058

Large, W. G., & Yeager, S. G. (2009). The global climatology of an interannually varying air–sea flux data set. *Climate Dynamics*, *33*, 341–364. https://doi.org/10.1007/s00382-008-0441-3

Lazier, J. (1980). Oceanographic conditions at ocean weather ship Bravo, 1964–1974. *Atmosphere-Ocean*, *18*(3), 227–238. https://doi.org/10.1080/07055900.1980.9649089

Lazier, J., Pickart, R., & Rhines, P. (2001). Chapter 5.5 Deep convection. In G. Siedler, J. Church, & J. Gould (Eds.), *Ocean Circulation and Climate* (pp. 387–400). Academic Press. https://doi.org/10.1016/S0074-6142(01)80130-3

Lohmann, K., Drange, H., & Bentsen, M. (2009). Response of the North Atlantic subpolar gyre to persistent North Atlantic oscillation like forcing. *Climate Dynamics*, *32*(2–3), 273–285. https://doi.org/10.1007/s00382-008-0467-6

Lozier, M. S., Bacon, S., Bower, A. S., Cunningham, S. A., de Jong, M. F., de Steur, L., et al. (2017). Overturning in the subpolar North Atlantic program. *Bulletin of the American Meteorological Society*, *98*(4), 737–752. https://doi.org/10.1175/BAMS-D-16-0057.1

Lozier, M. S., Li, F., Bacon, S., Bahr, F., Bower, A. S., Cunningham, S. A., et al. (2019). A sea change in our view of overturning in the subpolar North Atlantic. *Science*, *363*(6426), 516–521. https://doi.org/10.1126/science.aau6592

Luo, H., Castelao, R. M., Rennermalm, A. K., Tedesco, M., Bracco, A., Yager, P. L., & Mote, T. L. (2016). Oceanic transport of surface meltwater from the southern Greenland ice sheet. *Nature Geoscience*, *9*(7), 528–532. https://doi.org/10.1038/ngeo2708

Madec, G., Delecluse, P., Imbard, M., & Levy, C. (1998). OPA 8.1 ocean general circulation model reference manual. *Scientific Notes of Climate Modelling Center (11)*. Institut Pierre Simon Laplace (IPSL).

Madec, G., & NEMO System Team. (2016). NEMO Ocean Engine. *Scientific notes of climate modeling center (27)*. Institut Pierre Simon Laplace (IPSL). https://doi.org/10.5281/zenodo.1464816

Marshall, J., & Schott, F. (1999). Open-ocean convection: Observations, theory, and models. *Reviews of Geophysics*, *37*(1), 1–64. https://doi.org/10.1029/98RG02739

Martin, R., & Moore, G. W. K. (2007). Air-sea interaction associated with a Greenland reverse tip jet. *Geophysical Research Letters*, *34*(24), L24802. https://doi.org/10.1029/2007GL031093

Marzocchi, A., Hirschi, J. J. M., Holliday, N. P., Cunningham, S. A., Blaker, A. T., & Coward, A. C. (2015). The North Atlantic subpolar circulation in an eddy-resolving global ocean model. *Journal of Marine Systems*, *142*, 126–143. https://doi.org/10.1016/j.jmarsys.2014.10.007

Menary, M. B., Jackson, L. C., & Lozier, M. S. (2020). Reconciling the Relationship Between the AMOC and Labrador Sea in OSNAP Observations and Climate Models. *Geophysical Research Letters*, *47*, e2020GL089793. https://doi.org/10.1029/2020GL089793

Mertens, C., Rhein, M., Walter, M., Böning, C. W., Behrens, E., Kieke, D., et al. (2014). Circulation and transports in the Newfoundland Basin, western subpolar North Atlantic. *Journal of Geophysical Research: Oceans*, *119*(11), 7772–7793. https://doi.org/10.1002/2014JC010019

Mesinger, F., & Arakawa, A. (1976). Numerical methods used in atmospheric models. *Global Atmospheric Research Program World Meteorological Organization*, *1*(17), 1–66.

Monterey, G., & Levitus, S. (1997). *Seasonal variability of the global ocean mixed layer depth. NOAA Atlas NESDIS 14*. U.S. DEPARTMENT OF COMMERCE National Oceanic and Atmospheric Administration.

Nansen, F. (1912). *Das Bodenwasser und die Abkühlung des Meeres*. Internationale Revue Der Gesamten Hydrobiologie Und Hydrographie, 5(1), 1–42. https://doi.org/10.1002/iroh.19120050102

Oltmanns, M., Straneo, F., Moore, G. W. K., & Mernild, S. H. (2014). Strong downslope wind events in Ammassalik, Southeast Greenland. *Journal of Climate*, *27*(3), 977–993. https://doi.org/10.1175/JCLI-D-13-00067.1

Ortega, P., Robson, J., Sutton, R. T., & Andrews, M. B. (2017). Mechanisms of decadal variability in the Labrador Sea and the wider North Atlantic in a high-resolution climate model. *Climate Dynamics*, *49*(7–8), 2625–2647. https://doi.org/10.1007/s00382-016-3467-y

Paquin, J. P., Lu, Y., Higginson, S., Dupont, F., & Garric, G. (2016). Modelled variations of deep convection in the Irminger Sea during 2003–10. *Journal of Physical Oceanography*, *46*(1), 179–196. https://doi.org/10.1175/JPO-D-15-0078.1

Pennelly, C., & Myers, P. G. (2020). Introducing LAB60: A 1/60° NEMO 3.6 numerical simulation of the Labrador Sea. *Geoscientific Model Development*, *13*(10), 4959–4975. https://doi.org/10.5194/gmd-13-4959-2020

Pickart, R. S., Spall, M. A., Ribergaard, M. H., Moore, G. W. K., & Milliff, R. F. (2003). Deep convection in the Irminger Sea forced by the Greenland tip jet. *Nature*, *424*(6945), 152–156. https://doi.org/10.1038/nature01729

Pickart, R. S., Straneo, F., & Moore, G. W. K. (2003). Is Labrador Sea Water formed in the Irminger basin? *Deep-Sea Research Part I: Oceanographic Research Papers*, *50*(1), 23–52. https://doi.org/10.1016/S0967-0637(02)00134-6

Pickart, R. S., Våge, K., Moore, G. W. K., Renfrew, I. A., Ribergaard, M. H., & Davies, H. C. (2008). Convection in the western North Atlantic sub-polar gyre: Do small-scale wind events matter? In R. R. Dickson, J. Meincke, & P. Rhines (Eds.), *Arctic-Subarctic Ocean Fluxes: Defining the Role of the Northern Seas in Climate* (pp. 629–652). https://doi.org/10.1007/978-1-4020-6774-7_27

Piron, A., Thierry, V., Mercier, H., & Caniaux, G. (2016). Argo float observations of basin-scale deep convection in the Irminger sea during winter 2011–2012. *Deep-Sea Research Part I: Oceanographic Research Papers*, *109*, 76–90. https://doi.org/10.1016/j.dsr.2015.12.012

Piron, A., Thierry, V., Mercier, H., & Caniaux, G. (2017). Gyre-scale deep convection in the subpolar North Atlantic Ocean during winter 2014–2015. *Geophysical Research Letters*, *44*(3), 1439–1447. https://doi.org/10.1002/2016GL071895

Rattan, S., Myers, P. G., Treguier, A. M., Theetten, S., Biastoch, A., & Böning, C. (2010). Towards an understanding of Labrador Sea salinity drift in eddy-permitting simulations. *Ocean Modelling*, *35*(1–2), 77–88. https://doi.org/10.1016/j.ocemod.2010.06.007

Rhein, M., Fischer, J., Smethie, W. M., Smythe-Wright, D., Weiss, R. F., Mertens, C., et al. (2002). Labrador Sea Water: Pathways, CFC inventory, and formation rates. *Journal of Physical Oceanography*, *32*(2), 648–665. https://doi.org/10.1175/1520-0485(2002)032<0648:LSWPCI>2.0.CO;2

Rhein, M., Kieke, D., Hüttl-Kabus, S., Roessler, A., Mertens, C., Meissner, R., et al. (2011). Deep water formation, the subpolar gyre, and the meridional overturning circulation in the subpolar North Atlantic. *Deep-Sea Research Part II: Topical Studies in Oceanography*, *58*(17–18), 1819–1832. https://doi.org/10.1016/j.dsr2.2010.10.061

Rhein, M., Steinfeldt, R., Kieke, D., Stendardo, I., & Yashayaev, I. (2017). Ventilation variability of Labrador Sea Water and its impact on oxygen and anthropogenic carbon: A review. *Philosophical Transactions of the Royal Society A: Mathematical, Physical and Engineering Sciences*, *375*, 20160321. https://doi.org/10.1098/rsta.2016.0321

Rieck, J. K., Böning, C. W., & Getzlaff, K. (2019). The nature of eddy kinetic energy in the Labrador Sea: Different types of mesoscale eddies, their temporal variability, and impact on deep convection. *Journal of Physical Oceanography*, *49*(8), 2075–2094. https://doi.org/10.1175/JPO-D-18-0243.1

Rieck, J. K., Böning, C. W., Greatbatch, R. J., & Scheinert, M. (2015). Seasonal variability of eddy kinetic energy in a global high-resolution ocean model. *Geophysical Research Letters*, *42*(21), 9379–9386. https://doi.org/10.1002/2015GL066152

Rühs, S., Getzlaff, K., Durgadoo, J. V., Biastoch, A., & Böning, C. W. (2015). On the suitability of North Brazil Current transport estimates for monitoring basin-scale AMOC changes. *Geophysical Research Letters*, *42*(19), 8072–8080. https://doi.org/10.1002/2015GL065695

Sabine, C. L., Feely, R. A., Gruber, N., Key, R. M., Lee, K., Bullister, J. L., et al. (2004). The Oceanic Sink for Anthropogenic CO_2. *Science*, *305*(5682), 367–371. https://doi.org/10.1126/science.1097403

Sarafanov, A. (2009). On the effect of the North Atlantic Oscillation on temperature and salinity of the subpolar North Atlantic intermediate and deep waters. *ICES Journal of Marine Science*, *66*, 1448–1454. https://doi.org/10.1093/icesjms/fsp094

Sarafanov, A., Falina, A., Sokov, A., Zapotylko, V., & Gladyshev, S. (2018). Ship-based monitoring of the Northern North Atlantic Ocean by the Shirshov institute of oceanology. The main results. In M. G. Velarde, R. Y. Tarakanov, & A. V. Marchenko (Eds.), *The Ocean in Motion* (pp. 415–427). Springer. https://doi.org/10.1007/978-3-319-71934-4_25

Schubert, R., Biastoch, A., Cronin, M. F., & Greatbatch, R. J. (2018). Instability-driven benthic storms below the separated Gulf Stream and the North Atlantic Current in a high-resolution ocean model. *Journal of Physical Oceanography*, *48*(10), 2283–2303. https://doi.org/10.1175/JPO-D-17-0261.1

Schulze, L. M., Pickart, R. S., & Moore, G. W. K. (2016). Atmospheric forcing during active convection in the Labrador Sea and its impact on mixed-layer depth. *Journal of Geophysical Research: Oceans*, *121*(9), 6978–6992. https://doi.org/10.1002/2015JC011607

Severin, T., Conan, P., Durrieu de Madron, X., Houpert, L., Oliver, M. J., Oriol, L., et al. (2014). Impact of open-ocean convection on nutrients, phytoplankton biomass and activity. *Deep-Sea Research Part I Oceanographic Research Papers*, *94*, 62–71. https://doi.org/10.1016/j.dsr.2014.07.015

Sproson, D. A. J., Renfrew, I. A., & Heywood, K. J. (2008). Atmospheric conditions associated with oceanic convection in the south-east Labrador Sea. *Geophysical Research Letters*, *35*(6), L06601. https://doi.org/10.1029/2007GL032971

Steele, M., Morley, R., & Ermold, W. (2001). PHC: A global ocean hydrography with a high-quality Arctic Ocean. *Journal of Climate*, *14*, 2079–2087. https://doi.org/10.1175/1520-0442(2001)014<2079:PAGOHW>2.0.CO;2

Sutherland, D. A., Pickart, R. S., Jones, E. P., Azetsu-Scott, K., Eert, A. J., & Ólafsson, J. (2009). Freshwater composition of the waters off southeast Greenland and their link to the Arctic Ocean. *Journal of Geophysical Research: Oceans*, *114*(5), C05020. https://doi.org/10.1029/2008JC004808

Tagklis, F., Bracco, A., Ito, T., & Castelao, R. M. (2020). Submesoscale modulation of deep water formation in the Labrador Sea. *Scientific Reports*, *10*(1), 1–13. https://doi.org/10.1038/s41598-020-74345-w

Terenzi, F., Hall, T. M., Khatiwala, S., Rodehacke, C. B., & LeBel, D. A. (2007). Uptake of natural and anthropogenic carbon by the Labrador Sea. *Geophysical Research Letters*, *34*(6), L06608. https://doi.org/10.1029/2006GL028543

Tesdal, J. E., Abernathey, R. P., Goes, J. I., Gordon, A. L., & Haine, T. W. N. (2018). Salinity trends within the upper layers of the subpolar North Atlantic. *Journal of Climate*, *31*(7), 2675–2698. https://doi.org/10.1175/JCLI-D-17-0532.1

Tsujino, H., Urakawa, S., Nakano, H., Small, R. J., Kim, W. M., Yeager, S. G., et al. (2018). JRA-55 based surface dataset for driving ocean–sea-ice models (JRA55-do). *Ocean Modelling*, *130*, 79–139. https://doi.org/10.1016/j.ocemod.2018.07.002

Våge, K., Pickart, R. S., Moore, G. W. K., & Ribergaard, M. H. (2008). Winter Mixed Layer Development in the Central Irminger Sea: The Effect of Strong, Intermittent Wind Events. *Journal of Physical Oceanography*, *38*(3), 541–565. https://doi.org/10.1175/2007JPO3678.1

Våge, K., Pickart, R. S., Thierry, V., Reverdin, G., Lee, C. M., Petrie, B., et al. (2009). Surprising return of deep convection to the subpolar North Atlantic Ocean in winter 2007–2008. *Nature Geoscience*, *2*(1), 67–72. https://doi.org/10.1038/ngeo382

Visbeck, M., Chassignet, E. P., Curry, R. G., Delworth, T. L., Dickson, R. R., & Krahmann, G. (2003). The ocean's response to North Atlantic oscillation variability. In J. W. Hurrell, Y. Kushnir, G. Ottersen, & M. Visbeck (Eds.), *The North Atlantic Oscillation: Climatic Significance and Environmental Impact* (pp. 113–145). American Geophysical Union. https://doi.org/10.1029/134GM06

Yang, Q., Dixon, T. H., Myers, P. G., Bonin, J., Chambers, D., Van Den Broeke, M. R., et al. (2016). Recent increases in Arctic freshwater flux affects Labrador Sea convection and Atlantic overturning circulation. *Nature Communications*, *7*(1), 1–8. https://doi.org/10.1038/ncomms10525

Yashayaev, I. (2007). Hydrographic changes in the Labrador Sea, 1960-2005. *Progress in Oceanography*, *73*(3–4), 242–276. https://doi.org/10.1016/j.pocean.2007.04.015

Yashayaev, I., & Loder, J. W. (2016). Recurrent replenishment of Labrador Sea Water and associated decadal-scale variability. *Journal of Geophysical Research: Oceans*, *121*(11), 8095–8114. https://doi.org/10.1002/2016JC012046

Yashayaev, I., & Loder, J. W. (2017). Further intensification of deep convection in the Labrador Sea in 2016. *Geophysical Research Letters*, *44*(3), 1429–1438. https://doi.org/10.1002/2016GL071668

Zunino, P., Mercier, H., & Thierry, V. (2020). Why did deep convection persist over four consecutive winters (2015-2018) southeast of Cape Farewell? *Ocean Science*, *16*(1), 99–113. https://doi.org/10.5194/os-16-99-2020